3. GLOBAL OCEANS

a. Overview—G. C. Johnson

The global oceans transport, store, and exchange with the atmosphere vast amounts of heat, water, carbon dioxide, and other constituents vital to climate. This chapter describes, with a focus on 2017 conditions, seasonal to interannual variability of sea surface temperature; ocean heat content; salinity; air–sea fluxes of heat, freshwater, and momentum; sea level; surface currents; the Atlantic meridional circulation; phytoplankton; and ocean inorganic carbon cycling. It also puts 2017 conditions in a longer-term context.

Neutral to weak La Niña conditions that held for much of 2016 recurred in 2017, so sea surface temperatures (SSTs), ocean heat content (OHC), and sea level continued to rise in the western tropical Pacific and fall in the eastern tropical Pacific. A zonal band of westward surface current anomaly north of and along the equator played a role in the redistribution of warm near-surface waters from east to west. Sea surface salinity (SSS) freshened in the west and became saltier in the east. In the eastern equatorial Pacific chlorophyll-*a* and CO_2 flux from ocean to atmosphere were both elevated. All these tropical Pacific variations were consistent with 2016 to 2017 tendencies in regional wind stress and freshwater flux. There was a prominent band of anomalously high SST, OHC, and sea level as well as low SSS across much of the North Pacific between about 5° and 30°N in 2017. Effects included nuisance flooding in Hawaii.

Southeast of Greenland[1] SST, OHC, SSS, and sea level all remained below average in 2017, as they have since 2014. Along the east coast of North America SSTs, OHC, and sea level were all anomalously high in 2017, as they have generally been since at least 2009. In climate models this North Atlantic SST pattern is associated with a reduction in the Atlantic meridional overturning circulation.

In the Indian Ocean SST and SSS anomalies were both high in the west and below average in different parts of the east in 2017. Around the equator OHC fell in the west owing to a shoaling thermocline there. Anomalous eastward surface velocities around the equator in 2017 were likely associated with that shoaling thermocline and the high SSS anomalies there, with the latter owing partly to anomalous eastward advection of salty water. Sea level fell from 2016 to 2017 north of ~10°S in the Indian Ocean and rose south of that latitude.

Over the long term, as atmospheric CO_2 concentrations have risen, the ocean has taken up more carbon and acidified. Also on the long term, the 1993–2017 trends in OHC and sea level reflect statistically significant warming and sea level rise, especially in the Southern Hemisphere. Near the Antarctic Circumpolar Current a warming trend is evident in the Indian Ocean and western Pacific sectors of the Southern Ocean, but a cooling trend is discernible in the central Pacific sector.[2]

While the global average SST for 2017 was slightly below the 2016 value, the long-term trend is upward. The last three years have been the three highest annual values observed and have been associated with widespread coral bleaching. Both global average sea level and the global integrals of 0–700 m and 0–2000 m OHC reached record highs in 2017. Global integrals of OHC and global averages of sea level exhibit substantially less variable upward trends than that for SST. In haiku form:

Surface fluctuates,
ocean warms more steadily,
seas continue rise.

b. Sea surface temperatures—B. Huang, J. Kennedy, Y. Xue, and H.-M. Zhang

Global sea surface temperature (SST) and its changes are assessed mostly based on the Extended Reconstruction Sea-Surface Temperature version 5 (ERSSTv5; Huang et al. 2017) unless otherwise specified. The global integral of annually averaged SST anomaly (SSTA; relative to a 1981–2010 climatology) decreased slightly from a historic high of 0.40 (±0.06) °C in 2016 to 0.34 (±0.06) °C in 2017, although these values are not statistically distinguishable. The 95% confidence levels are estimated from a 1000-member ensemble of ERSSTv4 (Huang et al. 2016a).

Annually averaged SSTA in 2017 exceeded +0.5°C in the western tropical Pacific, subtropical North Pacific, western subtropical South Pacific, western tropical Indian Ocean, and eastern North Atlantic (Fig. 3.1a). SSTA values exceeded +1°C adjacent to the Arctic (in the Nordic, Barents, Chukchi, and Bering Seas; see Section 5e for a full description of Arctic SSTs), the northwestern North Atlantic southeast of Cape Cod, around the Korean Peninsula, the central southern Indian Ocean, and South Atlantic near the coasts of Argentina and Uruguay. In contrast, SSTA was slightly colder than average in the Southern

[1] Arctic and Nordic Seas SST and sea ice are discussed in Chapter 5.

[2] Southern Ocean conditions and sea ice are discussed in Chapter 6.

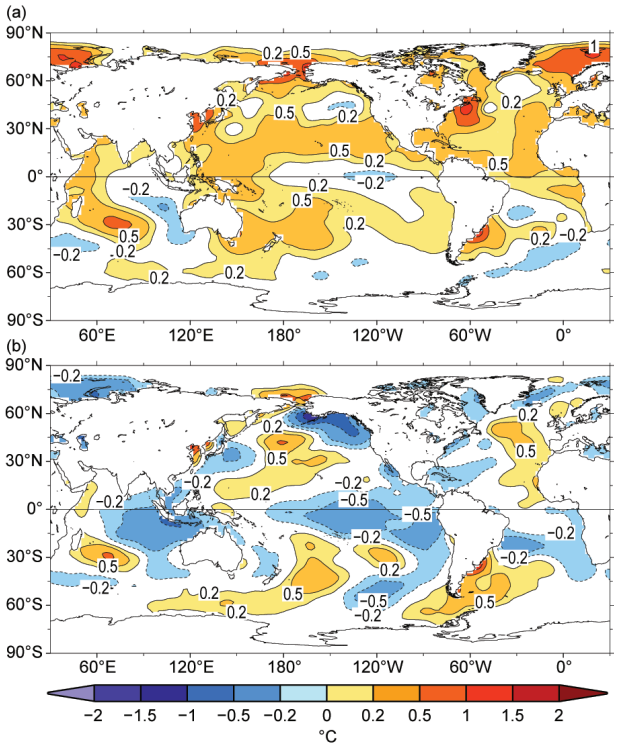

Fig. 3.1. (a) Annually averaged ERSSTv5 SSTA (°C) for 2017 relative to a 1981–2010 climatology and (b) difference of annually averaged SSTAs between 2017 and 2016 (2017–2016).

Hemisphere oceans, the central-eastern tropical Pacific, eastern North Pacific near 45°N, southeastern tropical Indian Ocean, and Southern Ocean south of 40°S in 60°W–60°E and 180°–120°W.

In comparison with 2016, SST in 2017 was mostly cooler in the tropical/subtropical oceans while warming in the midlatitudes (Fig. 3.1b). Specifically, the 2017 SST was 0.2°–0.5°C higher than 2016 in the central-to-southwestern North Pacific, central South Pacific, eastern North Atlantic, Chukchi Sea of the Arctic, western Indian Ocean, and Southern Ocean south of 40°S. In contrast, SST was 0.5°–1.0°C lower in the high-latitude North Pacific and 0.2°–0.5°C lower in the central-eastern tropical Pacific, western subtropical North Pacific, western North Atlantic, Arctic in the Atlantic sector, subtropical South Atlantic, and eastern Indian Ocean.

Cooling SST in the tropical Pacific and Indian Oceans in 2017 in comparison with 2016 (Figs. 3.1a,b) resulted from a shift from the strong 2015/16 El Niño to a weak La Niña in late 2016, with neutral conditions during most of 2017 and La Niña recurring later in 2017 (Fig. 3.2d; Ashok et al. 2003; Huang et al. 2016b; Xue and Kumar 2017; L'Heureux et al. 2017). In the eastern tropical Pacific near Peru, negative SSTAs reached −1σ (standard deviation derived from ERSSTv5 over 1981–2010) below average in SON 2017 (Fig. 3.2d), while SSTAs were extraordinarily high (+2σ) in DJF and MAM (Figs. 3.2a,b). In the western tropical Pacific, high SSTAs (+1 to +2σ) persisted throughout the year (Fig. 3.2), extending to the subtropical North Pacific over 10°–30°N. In the Indian Ocean, the SSTA pattern of warm (+1 to +2σ) in the west and cold (−1σ) in the east was sustained throughout all of 2017. This SST pattern resulted in a positive phase of the Indian Ocean dipole (IOD; Saji et al. 1999) in 2017 (Fig. 3.2), while the IOD was negative in 2016. The positive IOD in 2017 did not correspond with the development of the La Niña (Meyers et al. 2007).

In the North Pacific near 45°N, SST was 1σ colder than average in DJF (Fig. 3.2a), cold SSTA weakened in MAM and JJA (Figs. 3.2b,c), and SSTA reached +1σ near the dateline in SON (Fig. 3.2d). The pattern of +1σ SSTA near the dateline and weaker (< +1σ) SSTA east of the dateline resulted in a negative phase of the Pacific decadal oscillation (PDO; Mantua and Hare 2002) in JJA and SON (Figs. 3.2c,d), consistent with the development of La Niña conditions in the tropical

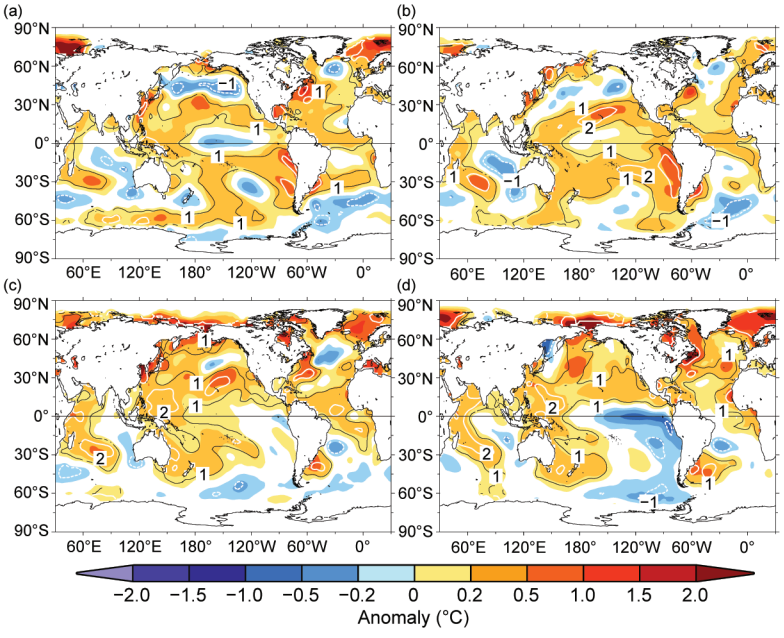

Fig. 3.2. Seasonally averaged SSTAs of ERSSTv5 (°C; colors) for (a) Dec 2016–Feb 2017, (b) Mar–May 2017, (c) Jun–Aug 2017, and (d) Sep–Nov 2017. Normalized seasonal mean SSTA based on seasonal mean std. dev. for 1981–2010 are indicated by contours of −1 (dashed white), +1 (solid black), and +2 (solid white).

Pacific. In the subtropical South Pacific, the SSTA was +1 to +2σ in DJF and MAM (Figs. 3.2a,b). The warm SSTA sustained in the west in JJA and SON, but diminished in the east (Figs. 3.2c,d) due to the development of the La Niña.

SSTAs were +1 to +2σ in most of the Atlantic (Fig. 3.2). SSTA in the Chukchi Sea was near neutral in DJF and MAM, and warmed to +2σ in JJA and SON. SSTA south of Greenland was below normal in DJF, MAM, and JJA (de Jong and de Steur 2016) but above normal in SON. SSTA from 20°–30°S was near neutral in DJF and MAM, and cooled in JJA and SON. Cold anomalies in the high-latitude Southern Ocean weakened from −1σ in DJF and MAM to near neutral in JJA and SON in the Atlantic sector (Figs. 3.2a,b), but strengthened from near neutral in DJF and MAM to −1σ in JJA and SON in the Pacific sector (Figs. 3.2c,d).

The long-term warming trend of globally averaged SST remained strong (Figs. 3.3a,b), although SST cooled slightly from 2016 to 2017. The linear trend of globally and annually averaged SSTA (for ERSSTv5) is 0.17 (±0.08) °C decade^{-1} from 2000 to 2017 and 0.10 (±0.01) °C decade^{-1} from 1950 to 2017 (Table 3.1), with 95% confidence levels. The higher trend for 2000 to 2017 indicates a potential accelerating warming in the modern period. The 2000 to 2017 warming trend for ERSSTv5 is consistent with those reported by Karl et al. (2015) and Hausfather et al. (2017) using ERSSTv4 data.

Warming of the global oceans from 2000 to 2017 (Table 3.1) was fast in the North Pacific (Fig. 3.3d) and tropical Indian Ocean (Fig. 3.3e) compared with the other regions (Fig. 3.3). Warming of the global oceans from 1950 to 2017 (Table 3.1) was nominally faster in the tropical Indian Ocean, tropical Atlantic, and North Atlantic; and slower in the tropical Pacific, Southern Ocean, and North Pacific.

In addition to the long-term SST trend, short-term SST variations can be seen in all global ocean basins, although their amplitude is typically smaller in the Southern Ocean. The variations associated with the Atlantic multidecadal oscillation (AMO; Wanner et al. 2001) in the North Atlantic can clearly be identified with warm periods during the 1930s–50s (not shown) and 1990s–2010s and a cold period during the 1960s–80s (Fig. 3.3f). From 2016 to 2017, annually averaged SSTA decreased in the Indian Ocean from 0.58°C to 0.35°C and decreased in the Pacific from 0.45°C to 0.39°C. However, annually averaged SSTA increased slightly in the Atlantic from 0.42°C to 0.43°C due to strong warming in the eastern North Atlantic, and it increased slightly from −0.11°C to −0.08°C in the Southern Ocean south of 45°S.

SSTs in ERSSTv5 are compared with those in the high-resolution satellite-based daily optimum

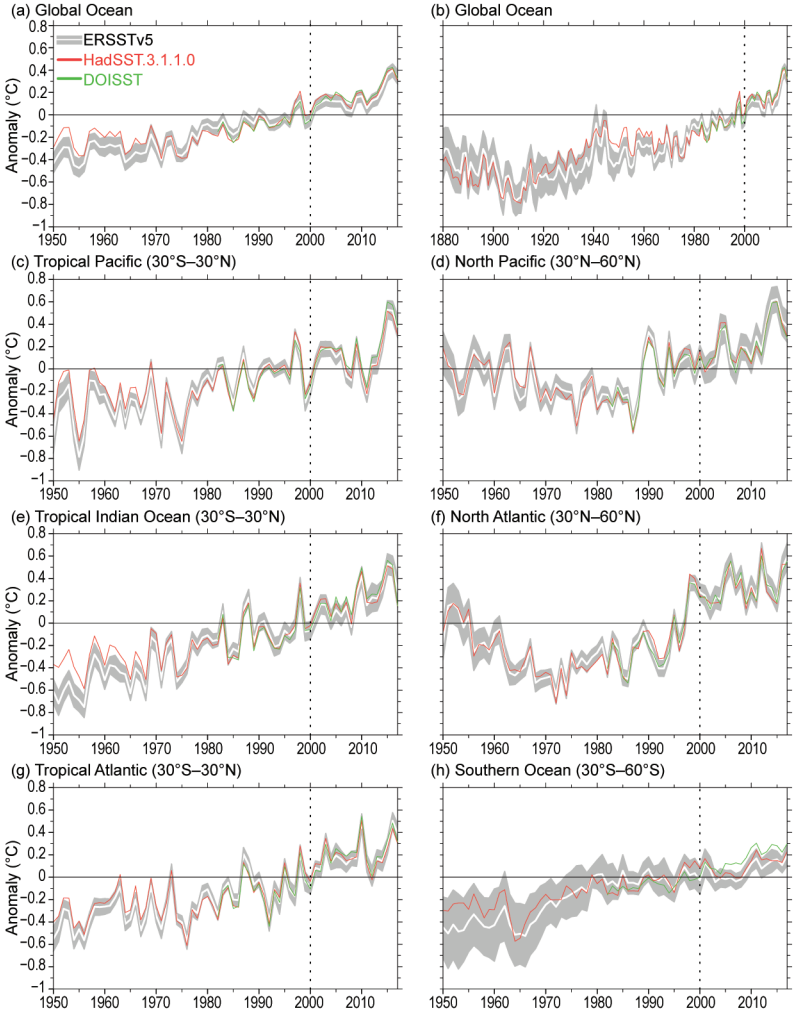

Fig. 3.3. Annually averaged SSTAs from ERSSTv5 (white line) with 2σ std. dev. (gray shading) of ERSSTv4, DOISST (green line), and HadSST.3.1.1.0 (red line) from 1950 to 2017 except for (b). (a) global ocean, (b) global ocean from 1880 to 2017, (c) tropical Pacific, (d) North Pacific, (e) tropical Indian, (f) North Atlantic, (g) tropical Atlantic, and (h) Southern Oceans. The year 2000 is indicated by a vertical black dotted line.

Table 3.1. Linear trends (°C decade^{-1}) of annually averaged SSTAs from ERSSTv5 except for global averaged SSTAs from HadSST3 and DOISST. The uncertainty at 95% confidence level are estimated by accounting for AR(1) effect on the degrees of freedom of annually averaged SST series.

	2000–2017	1950–2017
HadSST.3.1.1.0, Global	0.137 ± 0.078	0.083 ± 0.017
DOISST, Global	0.180 ± 0.067	N/A
ERSSTv5, Global	0.166 ± 0.082	0.099 ± 0.011
Tropical Pacific (30°S–30°N)	0.188 ± 0.192	0.100 ± 0.024
North Pacific (30°–60°N)	0.268 ± 0.135	0.062 ± 0.031
Tropical Indian Ocean (30°S–30°N)	0.240 ± 0.084	0.143 ± 0.016
North Atlantic (30°–60°N)	0.118 ± 0.100	0.102 ± 0.042
Tropical Atlantic (30°S–30°N)	0.158 ± 0.104	0.109 ± 0.018
Southern Ocean (30°–60°S)	0.103 ± 0.055	0.097 ± 0.014

interpolation SST (DOISST; Reynolds et al. 2007), and U.K. Met Office Hadley Centre SST version 3 (HadSST.3.1.1.0; Kennedy et al. 2011a,b), which uses a different algorithm from ERSSTv5 to correct ship SST observation bias. ERSSTv5 is a monthly SST product on a 2°×2° horizontal grid from 1854 to present based on in situ observations only (Huang et al. 2017). It builds upon ERSSTv4 (Huang et al. 2015) with more ship and buoy observations and the added ingestion of near-surface Argo observations. Biases in ship-based measurements are corrected using more accurate buoy observations. ERSSTv5 provides a better representation of spatial and temporal variations in high-latitude oceans and ENSO variability in the tropical Pacific than ERSSTv4. DOISST is a daily 0.25°×0.25° SST product for the modern satellite era from September 1981 to present using both in situ and satellite observations. HadSST.3.1.1.0 is a monthly 5°×5° SST product from 1850 to present using in situ observations only. All datasets are averaged to monthly 2°×2° grids for comparison purposes.

Comparisons (Fig. 3.3) indicate that SSTA deviations of DOISST and HadSST.3.1.1.0 from ERSSTv5 are largely within 2σ (gray shading in Fig. 3.3), as derived from a 1000-member ensemble analysis of ERSSTv4 (Huang et al. 2016a) and centered on ERSSTv5 SSTA. However, SSTAs are slightly higher in the 1950s–70s and 1920s–30s in HadSST.3.1.1.0 than in ERSSTv5 (Fig. 3.3b). Additionally, SSTAs are slightly higher in the 2000s–10s in HadSST.3.1.1.0 and DOISST than in ERSSTv5, particularly in the Southern Ocean. Therefore, SST trends are slightly weaker in HadSST.3.1.1.0 for both 1950 to 2017 and 2000 to 2017 (Table 3.1). In contrast, SST trends are slightly higher in DOISST from 2000 to 2017. These SSTA differences are mostly attributed to differences in ship-based observation bias corrections in different products (Huang et al. 2015; Kent et al. 2017).

c. Ocean heat content— G. C. Johnson, J. M. Lyman, T. Boyer, L. Cheng, C. M. Domingues, J. Gilson, M. Ishii, R. Killick, D. Monselesan, S. G. Purkey, and S. E. Wijffels

Storage and transport of heat in the ocean are central to aspects of climate such as ENSO (Johnson and Birnbaum 2017), tropical cyclones (Goni et al. 2009), sea level rise (Section 3f), variations in the global average surface warming rate (Xie et al. 2016), melting of ice sheet outlet glaciers around Greenland (Castro de la Guardia et al. 2015) and Antarctica (Schmidtko et al. 2014), and coral bleaching (Sidebar 3.1). Ocean warming accounts for about 93% of the total increase in Earth's energy storage from 1971 to 2010 (Rhein et al. 2013).

Maps of annual (Fig. 3.4) upper (0–700 m) ocean heat content anomaly (OHCA) relative to a 1993–2017 baseline mean are generated from a combination of in situ ocean temperature data and satellite altimetry data following Willis et al. (2004), but using Argo (Riser et al. 2016) data downloaded in January 2018. Near-global average seasonal temperature anomalies (Fig. 3.5) vs. pressure from Argo data (Roemmich and Gilson 2009, updated) since 2004 and in situ global estimates of OHCA (see Fig. 3.6) for three pressure layers from six different research groups (including those responsible for the 2000–6000-m estimate) are also discussed.

The 2017 minus 2016 tendency of 0–700-m OHCA (Fig. 3.4b) shows increases in the western subtropical and tropical North Pacific, with strong bands extending east-southeastward from Papua New Guinea and east-northeastward from the Philippines. These bands are reminiscent of Rossby wave signatures, which propagate westward more quickly closer to the equator (Chelton and Schlax 1996). Decreases are observed in portions of the central South Pacific and eastern North Pacific, as well as in the eastern equatorial Pacific around the latitude of the ITCZ.

Throughout much of the Pacific, the 2017 upper OHCA is generally above the long-term average, with the most prominent below-average region in the central South Pacific (Fig. 3.4a). A prominent band of high OHCA from about 5° to 30°N in 2017

is associated with anomalously high sea level (see Fig. 3.16), with impacts that include nuisance flooding in Hawaii (Sidebar 3.2). The Bering Sea, the Sea of Okhotsk, and especially the Yellow Sea and the Sea of Japan all exhibited anomalously high OHCA values in 2017. The 2017 0–700-m OHCA anomalies (Fig. 3.4a) are slightly above the 1993–2017 average in the western tropical Pacific, and below that average in the eastern tropical Pacific on both sides of the equator. This reverses a pattern that had held since 2014 (see previous *State of the Climate* reports) and is also reflected in sea level (see Fig. 3.16).

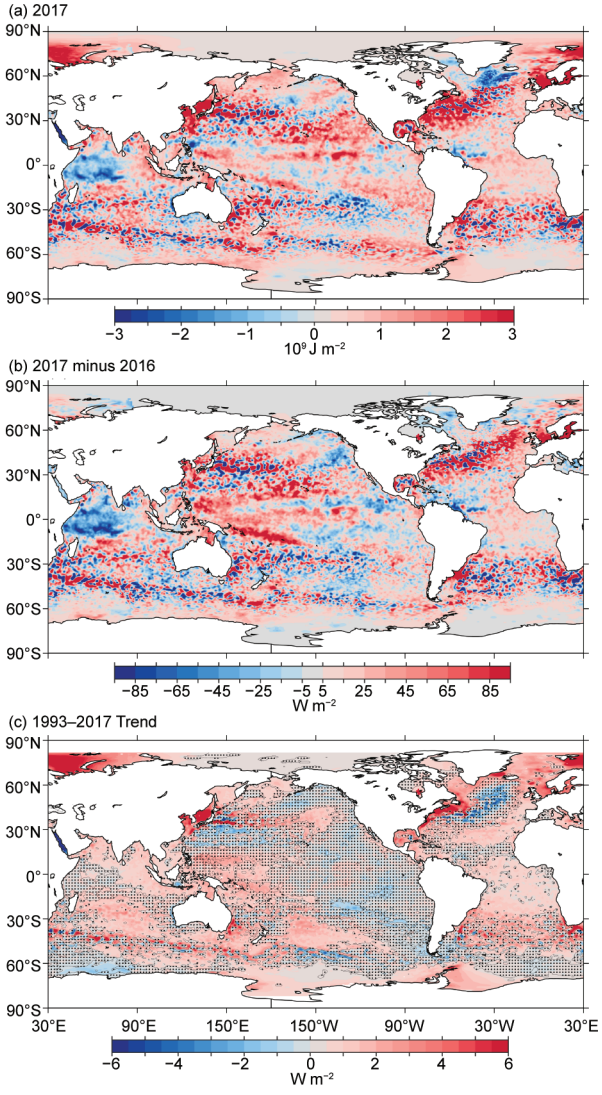

Fig. 3.4. (a) Combined satellite altimeter and in situ ocean temperature data estimate of upper (0–700 m) OHCA (× 10^9 J m^{-2}) for 2017 analyzed following Willis et al. (2004), but using an Argo monthly climatology and displayed relative to the 1993–2017 baseline. (b) 2017 minus 2016 combined estimates of OHCA expressed as a local surface heat flux equivalent (W m^{-2}). For (a) and (b) comparisons, note that 95 W m^{-2} applied over one year results in a 3 × 10^9 J m^{-2} change of OHCA. (c) Linear trend for 1993–2017 of the combined estimates of upper (0–700 m) annual OHCA (W m^{-2}). Areas with statistically insignificant trends are stippled.

In the Indian Ocean, the 2017 minus 2016 tendency of 0–700-m OHCA (Fig. 3.4b) exhibited strong cooling in the western equatorial region. This cooling was caused by a shoaling of the thermocline, which had little expression in SST (see Fig. 3.1), but was reflected in a reduction in SSH (see Fig. 3.16b) and likely effected by anomalous eastward flow in 2017 around the equator (see Fig. 3.18a). Near-surface salinity also increased in the western Indian Ocean (see Figs. 3.7b and 3.10c) during 2017, so the SSH reductions may be larger than would be expected from the cooling alone. There was also some warming south of 10°S and in much of the eastern Indian Ocean along with a large tendency toward higher values in a zonal band around 40°S in the Indian sector of the Southern Ocean. Upper OHCA values for 2017 were above the 1993–2017 mean in much of the Indian Ocean (Fig. 3.4a), with the notable exception of the formation of a large patch of low values in the western equatorial region discussed above.

There was a 2017 minus 2016 tendency toward higher values of 0–700-m OHCA (Fig. 3.4b) in the western subtropical and eastern subpolar North Atlantic, along with a slight increase throughout much of the tropics and a strong increase in a patch at about 35°S adjacent to South America. Weak decreases from 2016 to 2017 were apparent in the western tropical North Atlantic and in the subpolar region around Greenland. Much of the western North Atlantic from the Tropic of Capricorn to about 50°N had anomalously high upper OHCA values in 2017 (Fig. 3.4a), as did much of the Gulf of Mexico, the western Caribbean Sea, and the Greenland–Iceland–Norwegian Seas. The warm conditions off the east coast of North America have generally been present since 2009 (see previous *State of the Climate* reports). The only large region in the entire Atlantic with 2017 values well below the 1993–2017 mean was south of Greenland, especially in the Irminger Sea; a pattern that has persisted since at least 2014.

Regions around all the subtropical western boundary current extensions: the Kuroshio and the East Australian Current in the Pacific, the Agulhas retroflection in the Indian Ocean, and the Gulf Stream and the Brazil Current in the Atlantic all displayed anomalously high upper OHCA in 2017 (Fig. 3.4a). A trend toward higher values is also statistically significant from 1993 to 2017 in all these boundary currents (Fig. 3.4c), consistent with previous analysis (Wu et al. 2012).

Other large-scale statistically significant (Fig. 3.4c) regional patterns in the 1993–2017 local linear trends of upper OHCA reflect a warming trend in much of the Southern Hemisphere (Roemmich et al. 2015; Wijffels et al. 2016). In addition, there are significant positive trends in much of the tropical Atlantic and North Indian Oceans, as well as all of the marginal seas except the Red Sea. The strongest negative trends are found in the North Pacific south of the Kuroshio Extension and in the North Atlantic south

SIDEBAR 3.1: UNPRECEDENTED THREE YEARS OF GLOBAL CORAL BLEACHING 2014–17—C. M. EAKIN, G. LIU, A. M. GOMEZ, J. L. DE LA COURI, S. F. HERON, W. J. SKIRVING, E. F. GEIGER, B. L. MARSH, K. V. TIRAK, AND A. E. STRONG

Continued ocean warming has taken a severe toll on tropical coral reefs worldwide as heat stress has caused repeated bleaching and disease outbreaks (Eakin et al. 2009). Bleaching occurs when stress to the coral–algal symbiosis causes corals to expel endosymbiotic algae and, if prolonged or particularly severe, can result in partial or complete coral mortality (Brown 1997). While many stressors can cause bleaching, "mass" coral bleaching (covering hundreds of kilometers or more) is primarily driven by prolonged anomalously warm ocean temperatures coupled with high subsurface light levels, exceeding corals' physiological tolerances. Heat stress causing mass coral bleaching can be monitored accurately by satellites (G. Liu et al. 2014, 2017) and has increased in frequency and severity with a warming climate (Hughes et al. 2018).

Past mass bleaching events usually have been limited to El Niño years: the first in 1983 (Glynn 1990; Coffroth et al. 1990) was followed by the first recorded global event in 1998 and the second in 2010 (Heron et al. 2016b). The third global coral bleaching lasted three full years during 2014 to 2017 (NOAA 2017). This third global bleaching event was the longest, most widespread, and almost certainly most destructive on record. NOAA's Coral Reef Watch (CRW) defines global coral bleaching events as those with coral bleaching spanning hundreds of kilometers or more in all three ocean basins.

The third global bleaching event started in June 2014, when El Niño formation was expected but never fully materialized (Blunden and Arndt 2015). CRW satellite monitoring first detected heat stress sufficient to cause coral bleaching (Alert Level 1, defined in Fig. SB3.1) in Guam and the Commonwealth of the Northern Mariana Islands (CNMI; Heron et al. 2016a). An anomalously warm North Pacific Ocean brought severe heat stress to parts of the Northwestern Hawaiian Islands (Couch et al. 2017) and the Marshall Islands in the central Pacific (Fellenius 2014) and moderate stress to the main Hawaiian Islands (DAR 2014; Bahr et al. 2015). Teleconnected warming then brought heat stress to Florida (FRRP 2015).

Despite El Niño formation being delayed until March (Blunden and Arndt 2016), 2015 followed the classic pattern and sequence of heat stress and bleaching (Fig. SB3.1a) seen during the second year of an El Niño during prior global bleaching events (Hoegh-Guldberg 1999). Papua New Guinea and Fiji reported moderate heat stress and bleaching early in 2015 (Alert Level 1; Fig. SB3.1a); American Samoa reported its worst bleaching ever with widespread Alert Level 2 conditions. CRW documented moderate heat stress in the Indian Ocean, which spread to the Chagos Archipelago, Red Sea, and western Indonesia (Eakin et al. 2016). With the El Niño's onset, SST anomalies in the central and eastern tropical Pacific

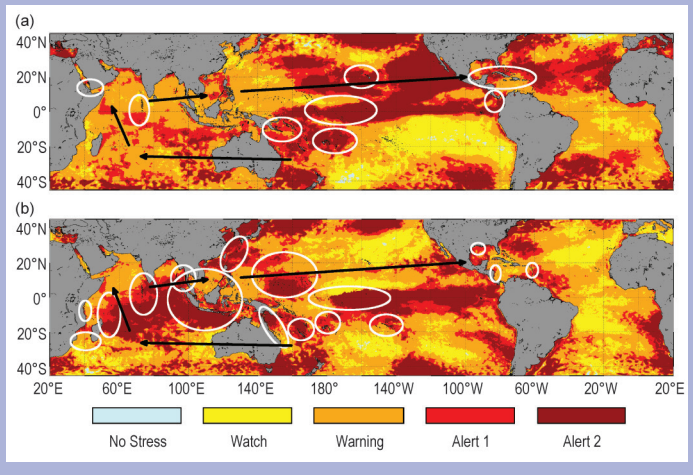

Fig. SB3.1. Evolution of and maximum heat stress for (a) 2015 and (b) 2016. Black lines show the annual pattern of heat stress from the South Pacific to the southern Indian Ocean, northern Indian Ocean and Southeast Asia, then to the Caribbean. Severe coral bleaching was reported from colleagues in all areas circled in white. CRW Bleaching Alert Area categories are defined as:

No Stress, HotSpot ≤ 0;
Watch, 0 < HotSpot < 1;
Warning, 1 ≤ HotSpot and 0 < DHW < 4;
Alert 1, 1 ≤ HotSpot and 4 ≤ DHW < 8, coral bleaching likely;
Alert 2, 1 ≤ HotSpot and 8 ≤ DHW, widespread bleaching and significant coral mortality likely; where HotSpot is the positive SST anomaly compared to the maximum monthly mean climatology and DHW is the Degree Heating Week heat stress accumulated from 12 preceding weeks of HotSpot values (G. Liu et al. 2014). Data from CRW's Daily Global 5-km Coral Bleaching Heat Stress Monitoring Product Suite v.3 (G. Liu et al. 2017).

of Greenland. The apparent warming and cooling trends adjacent to Antarctica are located in both in situ and altimeter data-sparse regions and may not be robust. A statistically significant warming trend in the western tropical Pacific that was quite strong in 1993–2013 but had disappeared for 1993–2016 (see previous *State of the Climate* reports) returned for 1993–2017, emphasizing the strong influence of El Niño and perhaps the PDO on sea level trends in that region (Merrifield et al. 2012), as well as the sen-

resulted in heat stress in the Line Islands at record levels (Fig. SB3.1a). Hawaii saw its worst bleaching ever (Rosinski et al. 2017). Florida's reefs experienced a second consecutive mass bleaching (FRRP 2016), and bleaching was reported on reefs across the eastern and western Caribbean (Eakin et al. 2016). With widespread bleaching observed in the Indian, Pacific, and Atlantic basins, NOAA declared in October 2015 the third global coral bleaching event was underway (NOAA 2015). By then, 41% of the world's coral reefs had experienced heat stress of 4°C-weeks (as defined in the caption of Fig. SB3.1a) or more, and almost all reefs had exceeded their normal warm-season temperatures.

With a strong El Niño in 2016, heat stress and bleaching returned to the Southern Hemisphere and followed the same global sequence as 2015—the first time this occurred in back-to-back years (Fig. SB3.1b). Heat stress in 2016 was much more widespread and intense than in 2015, encompassing 51% of coral reefs globally. Even more important was the severity. Continuous El Niño-related heat stress in the central Pacific for over a year caused the highest heat stress values CRW had ever documented. More than 25°C-weeks of heat stress in the Northern Line Islands killed 80% and bleached another 15% of corals in Kiritimati (Harvey 2016) and killed 98% of corals at Jarvis Island (Brainard et al. 2018). The first mass bleaching (85% bleached) of the northern and far-northern Great Barrier Reef (GBR; Hughes et al. 2017) killed 29% of the GBR's shallow-water corals (GBRMPA 2018). Widespread heat stress brought bleaching to much of the western Indian Ocean (CORDIO-EA 2016), including 69%–99% of corals bleached and 50% dead in the Seychelles (SIF 2017). CRW's forecasts of mass bleaching led Thailand to close many coral reef sites to diving (Agence France-Presse 2016). In the boreal summer, over 90% bleaching and 70% mortality were observed on Japan's largest reef (Harvey 2017); widespread bleaching also hit Guam again. Heat stress in the western Atlantic caused extensive bleaching in the western Caribbean and the worst bleaching ever seen in the Flower Garden Banks, located in the Gulf of Mexico (Johnston et al. 2017). Later, bleaching returned to the Marshall Islands in the central Pacific (Eakin et al. 2017).

Some South Pacific bleaching was reported in early 2017: mild in Fiji and severe in Niue, Samoa, and American Samoa. A second year of bleaching struck the GBR; this first-ever consecutive bleaching there focused on the northern and central sectors, killing another 22% of the GBR's corals (Hughes and Kerry 2017). Heat stress was limited in the Indian Ocean with moderate bleaching in southwestern Madagascar (CORDIO-EA 2016) and mild bleaching elsewhere. With a lack of widespread, severe Indian Ocean bleaching, NOAA declared the global event over as of May 2017 (NOAA 2017). However, bleaching still continued, with Guam and the CNMI experiencing widespread heat stress again. This was Guam's worst documented bleaching and fourth widespread event in five years.

Lasting an unprecedented 36 months, the third global event brought mass bleaching-level heat stress (Alert 1) to more than 75% of global reefs; nearly 30% also suffered mortality-level stress (Alert 2; Fig. SB3.2). More than half of affected reef areas were impacted at least twice. This global event has punctuated the recent acceleration of mass bleaching. Occurring at an average rate of once every 25–30 years in the 1980s, mass bleaching now returns about every six years and is expected to further accelerate as the oceans continue to warm (Hughes et al. 2018). Severe bleaching is now occurring more quickly than reefs can recover, with severe downstream consequences to ecosystems and people.

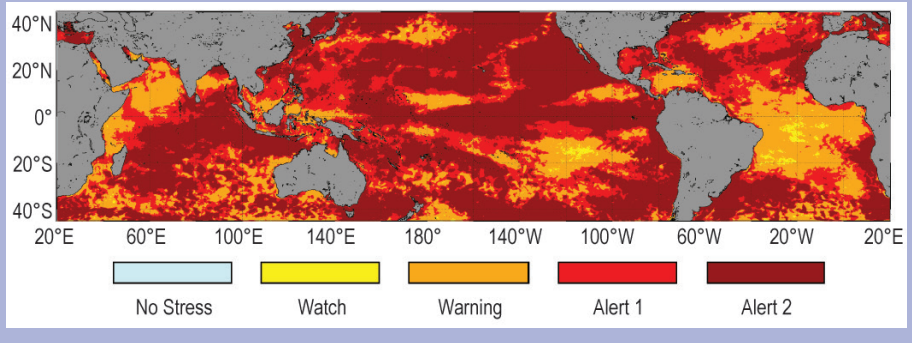

Fig. SB3.2. NOAA CRW Maximum Bleaching Alert Area map for Jun 2014–May 2017. Data from CRW's Daily Global 5-km Coral Bleaching Heat Stress Monitoring Product Suite v.3 (G. Liu et al. 2017).

sitivity of trends in relatively short records to choices of end points.

Near-global average monthly (smoothed to seasonal time-scale) temperature anomalies (Fig. 3.5a) reflect both a long-term warming trend (Fig. 3.5b, orange line) and ENSO redistributing heat (e.g., Roemmich and Gilson 2011) from the upper 100 dbar to a roughly 300-dbar thick layer just below. Lower temperature values are evident in the upper 100 dbar and higher values from 100 to 400 dbar during La Niña (e.g., 2008/09), and vice versa during El Niño (e.g., 2015/16). Since the peak of El Niño near the start of 2016, mean temperatures in the upper 100 dbar declined, but throughout 2017 they still remained above the long-term average. Negative anomalies from 150 to 400 dbar peaking around the start of 2016 also abated, such that the entire water column from 0 to 2000 dbar was warmer in 2017 than the 2004–17 average. The overall warming trend (Fig. 3.5b, orange line) from 2004 to 2017 exceeds 0.19°C decade^{-1} near the surface, declining to less than 0.03°C decade^{-1} below 180 dbar and about 0.01°C decade^{-1} by 2000 dbar. Removing a linear regression against the Niño-3.4 index (e.g., Johnson and Birnbaum 2017) results in a decadal warming trend (Fig. 3.5b, blue line) that is somewhat less than the simple linear trend near the surface and slightly larger from about 100 to 400 dbar.

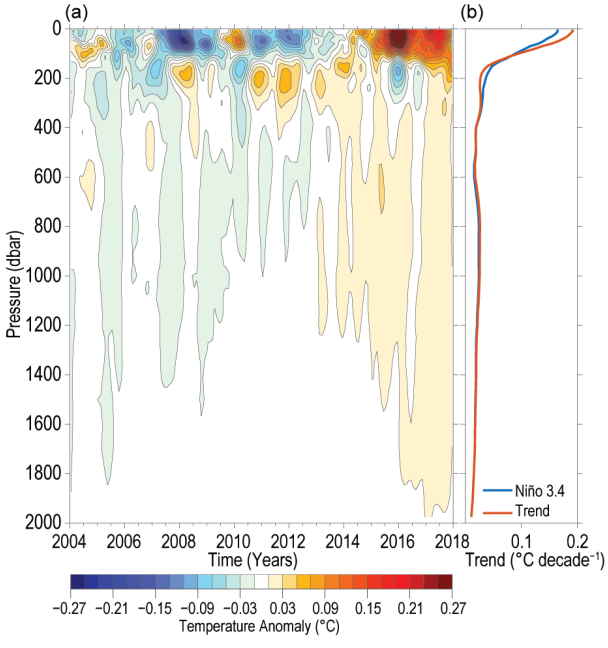

Fig. 3.5. (a) Near-global (65°S–80°N, excluding continental shelves, the Indonesian seas, the Sea of Okhostk, the Caribbean Sea, and the Gulf of Mexico) integrals of monthly ocean temperature anomalies [°C; updated from Roemmich and Gilson (2009)] relative to record-length average monthly values, smoothed with a 5-month Hanning filter and contoured at odd 0.02°C intervals (see colorbar) vs. pressure and time. (b) Linear trend of temperature anomalies over time for the length of the record in (a) plotted vs. pressure in °C decade^{-1} (orange line), and trend with a Niño-3.4 regression removed (blue line) following Johnson and Birnbaum (2017).

The analysis is extended back in time from the Argo period (which started in the early 2000s) to 1993, and deeper, using sparser, and more heterogeneous, historical data collected mostly from ships (e.g., Abraham et al. 2013). Six different estimates of glob-

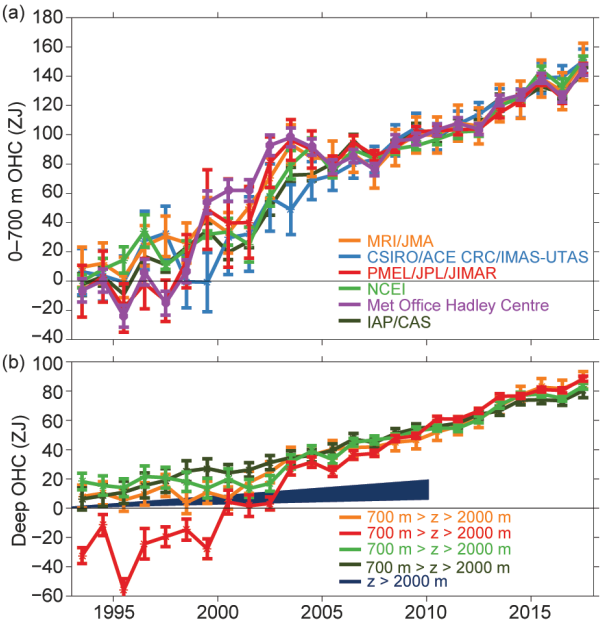

Fig. 3.6. (a) Annual average global integrals of in situ estimates of upper (0–700 m) OHCA (ZJ; 1 ZJ = 10^{21} J) for 1993–2017 with standard errors of the mean. The MRI/JMA estimate is an update of Ishii et al. (2017). The CSIRO/ACE CRC/IMAS-UTAS estimate is an update of Domingues et al. (2008). The PMEL/JPL/JIMAR estimate is an update and refinement of Lyman and Johnson (2014). The NCEI estimate follows Levitus et al. (2012). The Met Office Hadley Centre estimate is computed from gridded monthly temperature anomalies (relative to 1950–2016) following Palmer et al. (2007). The IAP/CAS estimate is described in Cheng et al. (2017). See Johnson et al. (2014) for details on uncertainties, methods, and datasets. For comparison, all estimates have been individually offset (vertically on the plot), first to their individual 2005–17 means (the best sampled time period), and then to their collective 1993 mean. (b) Annual average global integrals of in situ estimates of intermediate (700–2000 m) OHCA for 1993–2017 with standard errors of the mean, and a long-term trend with one standard error uncertainty shown from 1992–2010 for deep and abyssal (z > 2000 m) OHCA following Purkey and Johnson (2010) but updated using all repeat hydrographic section data available from https://cchdo.ucsd.edu/ as of Jan 2018.

ally integrated in situ 0–700-m OHCA (Fig. 3.6a) all reveal a large increase since 1993, with 2017 being a record high value. A similar pattern is apparent from 700 to 2000 m (Fig. 3.6b). While the trend in globally integrated ocean heat content is modulated by El Niño and is slowed or even reversed after El Niño peaks (Johnson and Birnbaum 2017), it, like globally averaged sea level (see Fig. 3.15a), exhibits a much steadier increase than globally averaged surface temperatures (see Fig. 3.3a). Globally integrated OHCA values vary more both from year-to-year for individual years and from estimate-to-estimate in any given year prior to the achievement of a near-global Argo array around 2005. Causes of differences among estimates are discussed in Johnson et al. (2015).

The rate of heat gain from linear trends fit to each of the six global integral estimates of 0–700 m OHCA from 1993 through 2017 (Fig. 3.6a) range from 0.36 (±0.06) to 0.40 (±0.18) W m^{-2} applied over the surface area of Earth (Table 3.2). Linear trends from 700 to 2000 m over the same time period range from 0.19 (±0.07) to 0.35 (±0.03) W m^{-2}. Trends in the 0–700-m layer all agree within uncertainties, and all but one of the four trends in the 700–2000-m layer do as well. For that layer the PMEL/JPL/JIMAR trend is larger than the others because it assumes the average anomaly in sampled regions applies globally (Lyman and Johnson 2014). For 2000–6000 m, the linear trend is 0.04 (±0.04) W m^{-2} from 1992 to 2010. Summing the three layers (with their slightly different time periods), the full-depth ocean heat gain rate ranges from 0.59 to 0.79 W m^{-2}.

Table 3.2. Trends of ocean heat content increase (in W m^{-2} applied over the 5.1 × 10^{14} m^2 surface area of Earth) from seven different research groups over three depth ranges (see Fig 3.6 for details). For the 0–700-m and 700–2000-m depth ranges, estimates cover 1993–2017, with 5%–95% uncertainties based on the residuals taking their temporal correlation into account when estimating degrees of freedom (Von Storch and Zwiers 1999). The 2000–6000-m depth range estimate, an update of Purkey and Johnson (2010), covers from 1992 to 2010, again with 5%–95% uncertainty.

Research group	Global ocean heat content trends (W m^{-2}) for three depth ranges		
	0–700 m	700–2000 m	2000–6000 m
MRI/JMA	0.36 ± 0.06	0.22 ± 0.06	—
CSIRO/ACE/CRC/IMAS/UTAS	0.40 ± 0.07	—	—
PMEL/JPL/JIMAR	0.40 ± 0.16	0.35 ± 0.03	—
NCEI	0.38 ± 0.07	0.19 ± 0.07	—
Met Office Hadley Centre	0.40 ± 0.18	—	—
ICCES	0.40 ± 0.06	0.19 ± 0.01	—
Purkey and Johnson update	—	—	0.04 ± 0.04

d. Salinity—G. C. Johnson, J. Reagan, J. M. Lyman, T. Boyer, C. Schmid, and R. Locarnini

1) Introduction—G. C. Johnson and J. Reagan

The ocean plays a large role in the global hydrological cycle, with the vast majority of evaporation and precipitation occurring over the oceans (e.g., Schanze et al. 2010). Ocean freshwater storage and transport, and variations thereof, are reflected in salinity patterns and their variations (e.g., Yu 2011). Where evaporation exceeds precipitation, such as in the subtropics, relatively salty surface waters are found. In contrast, where precipitation (and river run off) is greater than evaporation, such as under the ITCZs and in subpolar regions, fresher waters are present. In high latitudes, sea ice formation, advection, and melt also influences SSS (e.g., Petty et al. 2014). Subsurface ocean salinity patterns reflect the surface formation regions of water masses (e.g., Skliris et al. 2014), with fresher tropical waters overlying saltier subtropical waters, which in turn overlay fresher subpolar waters. Below these water masses lie the saltier North Atlantic Deep Water and below that the fresher Antarctic Bottom Water (Johnson 2008). North Atlantic Deep Water temperature and salinity vary over decades (e.g., Yashayaev and Loder 2016), whereas Antarctic Bottom Waters have been freshening in recent decades (e.g., Purkey and Johnson 2013). Salinity changes impact sea level changes (e.g., Durack et al. 2014) as well as the thermohaline circulation (e.g., W. Liu et al. 2017) and have been used to quantify changes in the hydrological cycle (e.g., Skliris et al. 2014).

To investigate interannual changes of subsurface salinity, all available salinity profile data are quality controlled following Boyer et al. (2013) and then used to derive 1° monthly mean gridded salinity anomalies relative to a long-term monthly mean for years 1955–2012 [World Ocean Atlas 2013 version 2 (WOA13v2); Zweng et al. 2013] at standard depths from the surface to 2000 m (Boyer et al. 2013). In recent years, the largest source of salinity profiles is the profiling floats of the Argo program (Riser et al. 2016). These data are a mix of real-time (preliminary) and delayed-mode (scientific quality controlled)

observations. Hence, the estimates presented here could change after all data have been subjected to scientific quality control. The SSS analysis relies on Argo data downloaded in January 2018, with annual maps generated following Johnson and Lyman (2012) as well as monthly maps of bulk (as opposed to skin) SSS data from BASS (Xie et al. 2014). BASS blends in situ SSS data with data from the *Aquarius* (Le Vine et al. 2014; mission ended in June 2015), SMOS (Soil Moisture and Ocean Salinity; Font et al. 2013), and recently SMAP (Soil Moisture Active Passive; Fore et al. 2016) satellite missions. BASS maps can be biased fresh around land (including islands) and at high latitudes. Despite the larger uncertainties of satellite data relative to Argo data, their higher spatial and temporal sampling allows higher spatial and temporal resolution maps than are possible using in situ data alone at present. Salinity is measured as a dimensionless quantity and reported on the 1978 Practical Salinity Scale, or PSS-78 (Fofonoff and Lewis 1979).

2) Sea surface salinity—G. C. Johnson and J. M. Lyman

Sea surface salinity anomalies outside of the tropics are fairly persistent, so 2017 SSS anomalies (Fig. 3.7a, colors) include some extratropical large-scale patterns that largely held from 2004 to 2016 (previous *State of the Climate* reports). Regions around the subtropical salinity maxima are generally salty with respect to WOA13v2, except in the North Pacific, where the salinity maximum is anomalously fresh in 2017. There are fresh anomalies relative to WOA13v2 in much of the high-latitude, low-salinity regions, primarily in portions of the subpolar gyres of the North Pacific and North Atlantic, and to a lesser extent around the Southern Ocean. These multiyear patterns are consistent with an increase in the hydrological cycle (e.g., more evaporation in drier locations and more precipitation in rainy areas) over the ocean, as expected in a warming climate (Rhein et al. 2013). A similar assertion could be made for some of the extratropical 2005–17 trends discussed below.

Tropical sea surface salinity changes from 2016 to 2017 (Fig. 3.7b, colors) are anti-correlated with 2016 to 2017 tendencies in precipitation minus evaporation ($P-E$; see Fig. 3.12b). The freshening in the off-equatorial western tropical Pacific and salinification around the equator in the west and under the ITCZ in the east are all well anti-correlated with $P-E$ tendencies, and associated with the transition from an El Niño that peaked around early 2016 to the neutral or weak La Niña conditions since then. A prominent example of the role of advection by anomalous ocean currents (see Fig. 3.18) in the 2016 to 2017 SSS tendencies is the increase in salinity in the equatorial Indian Ocean. This increase is associated with anomalous eastward currents, consistent with anomalous advection in the presence of mean SSS that decreases from west to east. Other prominent large-scale SSS changes from 2016 to 2017 include freshening in the northeast Pacific, the western tropical Atlantic, and around the equator across much of the Atlantic (Fig. 3.7b).

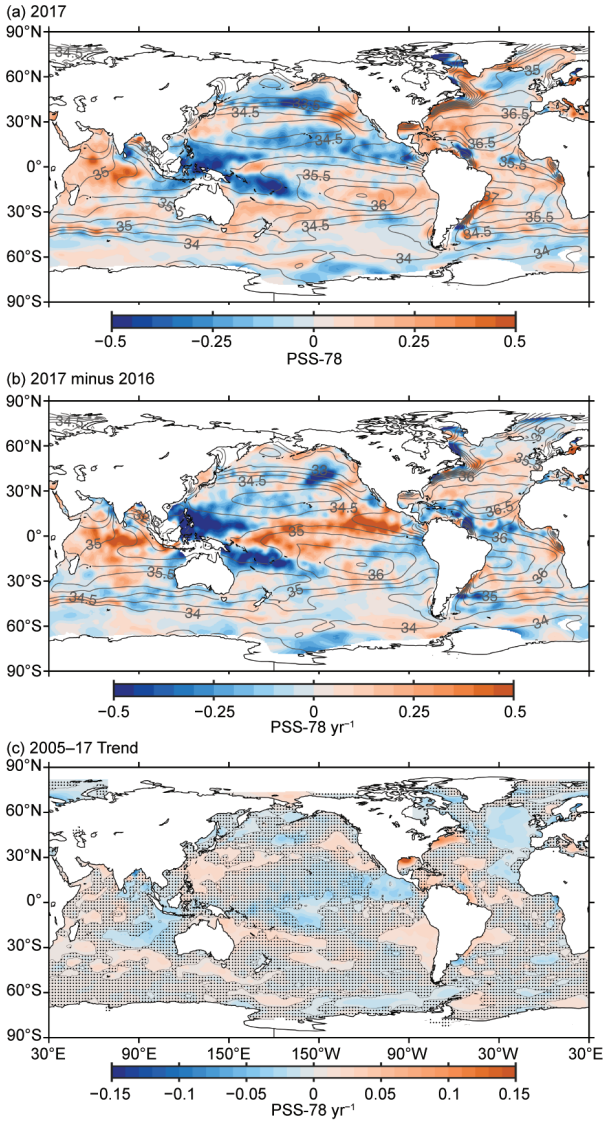

Fig. 3.7. (a) Map of the 2017 annual surface salinity anomaly (colors, PSS-78) with respect to monthly climatological 1955–2012 salinity fields from WOA13v2 [yearly average (gray contours at 0.5 intervals), PSS-78]. (b) Difference of 2017 and 2016 surface salinity maps (colors, PSS-78 yr^{-1}). White ocean areas are too data-poor (retaining < 80% of a large-scale signal) to map. (c) Map of local linear trends estimated from annual surface salinity anomalies for 2005–17 (colors, PSS-78 yr^{-1}). Areas with statistically insignificant trends are stippled. All maps are made using Argo data.

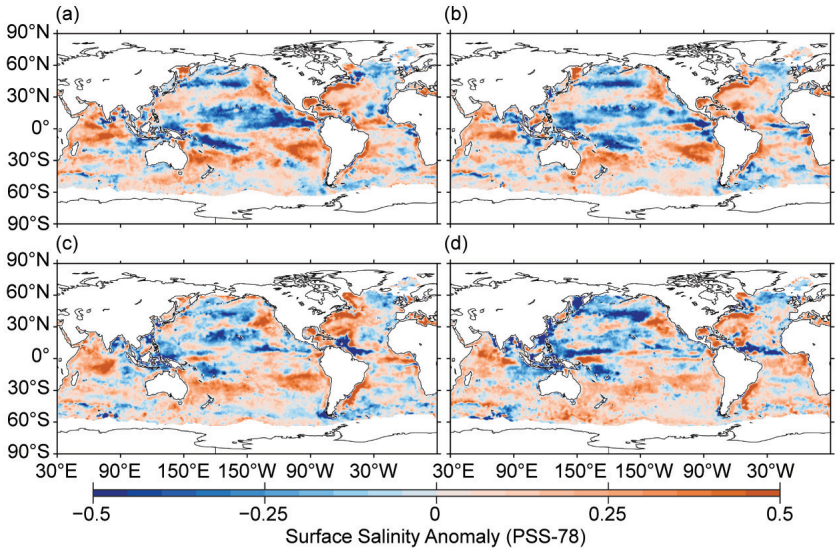

Fig. 3.8. Seasonal maps of SSS anomalies (colors) from monthly blended maps of satellite and in situ salinity data (BASS; Xie et al. 2014) relative to monthly climatological 1955–2012 salinity fields from WOA13v2 for (a) Dec–Feb 2016/17, (b) Mar–May 2017, (c) Jun–Aug 2017, and (d) Sep–Nov 2017. Areas with maximum monthly errors exceeding 10 PSS-78 are left white.

Strong seasonal variations of BASS (Xie et al. 2014) SSS anomalies (Fig. 3.8) are evident near the Amazon and Orinoco River plumes. While there is almost no fresh signal in December–February, a strong fresh anomaly extends north of the river mouths in March–May and grows to the north and extends eastward in June–August, with a strong fresh anomaly extending across much of the northern equatorial Atlantic in September–November. Other factors, including stronger-than-usual precipitation in the region (see Fig. 3.12), likely contributed to the fresh anomaly as well. In the tropical Pacific, fresh anomalies in the eastern Pacific warm pool diminished throughout the year while the western Pacific warm pool freshened, again consistent with the shift of precipitation to the western tropical Pacific after the 2015/16 El Niño and persistence of neutral and La Niña conditions throughout 2017.

Sea surface salinity trends for 2005–17 (Fig. 3.7c) are estimated by local linear fits to annual average SSS maps from Argo data. (The starting year is 2005 because that is when Argo coverage became near-global.) Regions with statistically significant increasing salinity trends are found near the subtropical salinity maxima in all the ocean basins, although the eastern subtropical North Atlantic is freshening, even near the salinity maximum. In the higher latitudes and the tropics, where mean salinity values are lower, there are some regions where the trend is toward freshening. In high latitudes, these freshening regions include the subpolar North Atlantic and North Pacific, as well as patches in the Pacific and Atlantic sectors of the Southern Ocean. In the tropics, they include the central Pacific, at the eastern edge of the western fresh pool, and in the warm fresh pool of the northeastern equatorial Pacific. There are also freshening trends in the already fresh Bay of Bengal, and a large patch west of Indonesia and Australia that has been present since at least 2009 (see previous *State of the Climate* reports). The regions to the northwest of the Gulf Stream and in the northern Gulf of Mexico are also trending strongly saltier, as well as warmer (Section 3c).

3) Subsurface salinity—J. Reagan, T. Boyer, C. Schmid, and R. Locarnini

For the first time in the past decade, nearly all 2017 Atlantic Ocean basin-average monthly salinity anomalies were positive from 0 to 1500 m (Fig. 3.9a). The year 2017 continued the same Atlantic salinity anomaly pattern that has been evident since 2008 with strong positive (> 0.05) near-surface salinity anomalies that weaken with depth (~0.005 at 700 m) (Fig. 3.9a). Salinity increased at nearly all depths within 0–1500 m from 2016 to 2017 (Fig. 3.9b) with the highest increase between 100 and 125 m (~0.017).

The 2017 Pacific Ocean basin-average salinity anomalies continued the same pattern that began in mid-2014 with fresh anomalies from 0 to 75 m, salty anomalies from 100 to 200 m, and fresh anomalies from 200 to 600 m (Fig. 3.9c). This marks the third straight year (2015–17) in which the upper ~75 m of the Pacific Ocean has been fresher than the long-term average. Previously, this layer had been saltier than the long-term average for five straight years (2009–13; Fig. 3.9c). These basin-average multiyear near-surface salinity shifts may be related to in-phase transitions of both ENSO and the PDO and their associated precipitation (Lau and Yang 2002) and equatorial wind stress/Ekman upwelling changes (Wang et al. 2015). From 2016 to 2017 the upper 125 m of the Pacific became fresher (max of ~ −0.018 at 0 m), while the 150–400-m layer became saltier (max of ~0.013 at 200 m; Fig. 3.9d).

From mid-2016 through 2017 the upper 200 m of the Indian Ocean became very salty (> 0.05 near the surface) when compared to the long-term mean

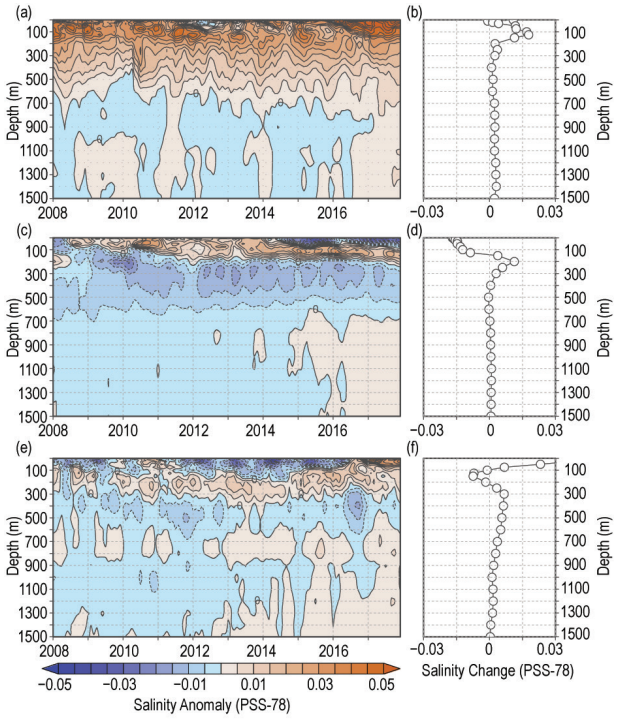

Fig. 3.9. Average monthly salinity anomalies (PSS-78) relative to the long-term WOA13v2 monthly salinity climatology for years 1955–2012 (Zweng et al. 2013) from 0 to 1500 m for the (a) Atlantic for 2008–17 and (b) the change from 2016 to 2017; (c) Pacific for 2008–17 and (d) the change from 2016 to 2017; (e) Indian for 2008–17 and (f) the change from 2016 to 2017. Data were smoothed using a 3-month running mean.

(Fig. 3.9e). Much of the surface of the Indian Ocean experienced salty anomalies (Fig. 3.7a) that were not driven directly by changes in $P-E$ (see Fig. 3.12a) but were due to anomalous ocean currents (see Fig. 3.18a and Section 3d2). Unsurprisingly, there was a large (~0.05 at 0 m; Fig. 3.9f) salinification of the near-surface from 0 to 100 m between 2016 and 2017, with freshening from 100 to 200 m, and salinification from 200 to 1000 m (Fig. 3.9f).

Most of the large (> |0.09|) zonally averaged salinity changes from 2016 to 2017 in the Atlantic occurred in the North Atlantic (Fig. 3.10a). There was freshening in the upper 50 m from 0° to 20°N, with maximum freshening (< −0.12) at ~10 m depth. This is in contrast to the salinification that was observed in this region between 2015 and 2016 (see Fig. 3.10a in Reagan et al. 2017). The freshwater discharge from the Amazon and Orinoco Rivers are likely the source of this freshening (Figs. 3.7b and 3.8a–d) with a stronger 2017 North Brazil Current (when compared to 2016) from March through August (see Figs. 3.19b,c) helping advect the freshwater river discharge farther to the north and northwest. Increased $P-E$ (see Fig. 3.12a) over the Atlantic ITCZ may have also played a role in the freshening over this area. North of this freshening, there was salinification (> 0.03) between 2016 and 2017 from 20° to 52°N, which expanded and deepened from the surface to 100 m at 20°N to 400 m at 50°N with maximum salinification (> 0.09) occurring at 50 m at 47.5°N.

The zonally averaged Pacific salinity changes from 2016 to 2017 are primarily concentrated in the upper 150 m (Fig. 3.10b). Near-surface (0–50 m) freshening (< −0.03) at 22°S extends equatorward and deepens to 150 m at 8°S with maximum freshening (< −0.12) at the surface near 15°S. This is a reversal of the salinification that took place from 2015 to 2016 in this area, and it is likely due to the transition from the strong El Niño in early 2016 to the neutral and weak La Niña conditions that dominated 2017 and its associated precipitation tendencies from 2016 to 2017 (see

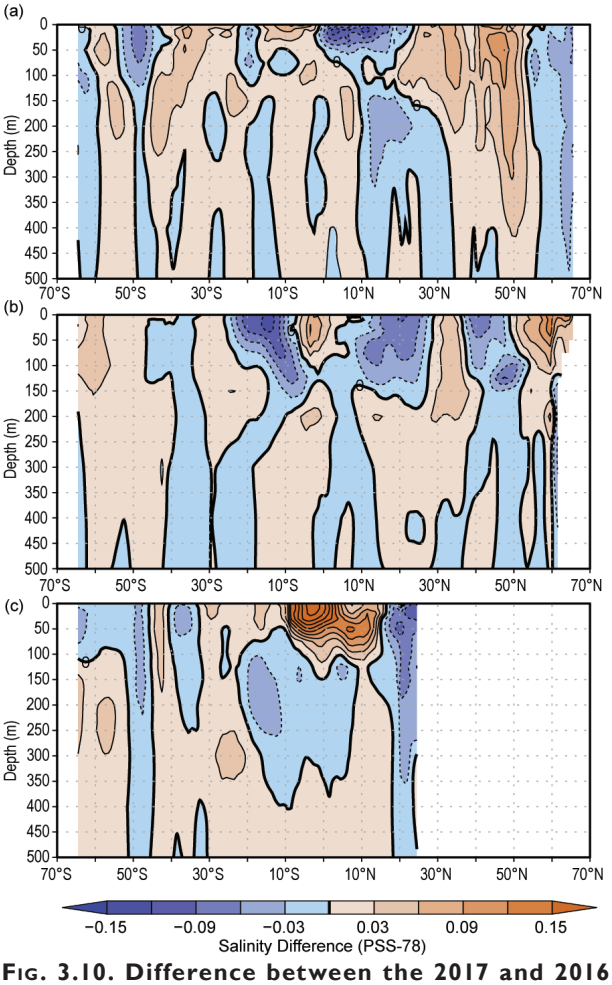

Fig. 3.10. Difference between the 2017 and 2016 zonal average monthly salinity anomalies (PSS-78) relative to the long-term WOA13v2 monthly salinity climatology for 1955–2012 (Zweng et al. 2013) from 0 to 500 m for the (a) Atlantic, (b) Pacific, and (c) Indian Ocean basins. Contours are multiples of ±0.03 with a bold 0 contour.

Fig. 3.12d). Near the equator, salinity increased between 2016 and 2017, likely due to the aforementioned ENSO transition and upwelling of higher salinity water caused by increased zonal wind stress from 2016 to 2017 (see Fig. 3.13b). Farther north there was freshening (< −0.03) from 10° to 27°N reaching a depth of ~140 m and freshening (< −0.03) between 38° and 50°N from 0 to 150 m. Finally, there was salinification (> 0.03) between 50° and 60°N in the upper 100 m.

The largest changes in zonally averaged salinity between 2016 and 2017 in the Indian Ocean occurred in the upper 100 m between 10°S and 15°N (Fig. 3.10c). In this region, there was broad-scale salinification (> 0.03) with large increases in salinity (> 0.20) in the upper 50 m between 10°S and the equator. As was discussed previously in this section, this salinification was primarily due to the advection of salty water via 2017 anomalous ocean currents (see Fig. 3.18a). Freshening (< −0.03) from 2016 to 2017 from 17° to 24°N extends down to 350 m and is primarily caused by the near-coast freshening along India's west coast (Fig. 3.7b).

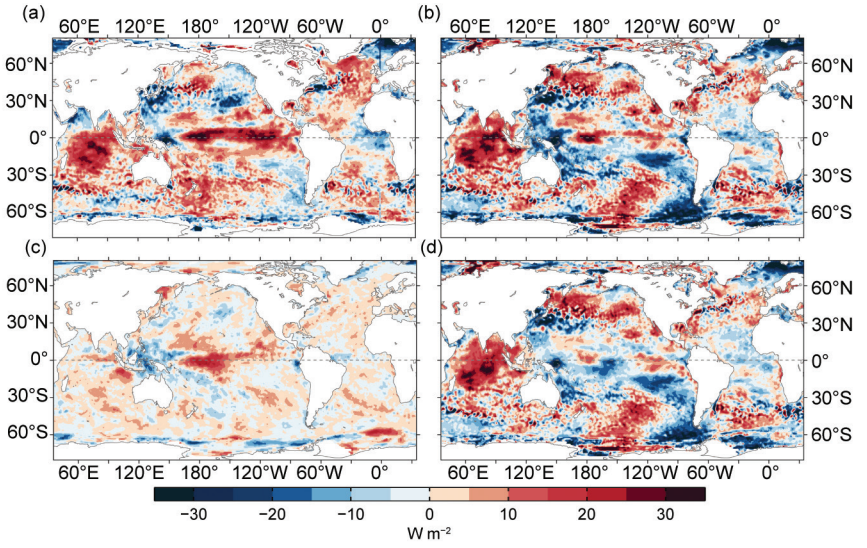

Fig. 3.11. (a) Surface heat flux (Q_{net}) anomalies (W m^{-2}) for 2017 relative to the 2010–14 mean. Positive values denote ocean heat gain. 2017 minus 2016 difference for (b) Q_{net}, (c) surface radiation (SW+LW), and (d) turbulent heat fluxes (LH+SH), respectively. Positive differences denote more ocean heat gain in 2017 than in 2016. LH+SH are produced by the OAFlux high-resolution (HR) satellite-based analysis, and SW+LW by the NASA FLASHFlux project.

e. *Global ocean heat, freshwater, and momentum fluxes*—L. Yu, X. Jin, S. Kato, N. G. Loeb, P. W. Stackhouse, R. A. Weller, and A. C. Wilber

The ocean and the atmosphere communicate via interfacial exchanges of heat, freshwater, and momentum. These air–sea fluxes are the primary mechanisms for keeping the global climate system nearly balanced with the incoming insolation at Earth's surface. Most of the shortwave radiation (SW) absorbed by the ocean's surface is vented into the atmosphere by three processes: longwave radiation (LW), turbulent heat loss by evaporation (latent heat flux, or LH), and conduction (sensible heat flux, or SH). The residual heat is stored in the ocean and transported by ocean circulation, forced primarily by the momentum transferred to

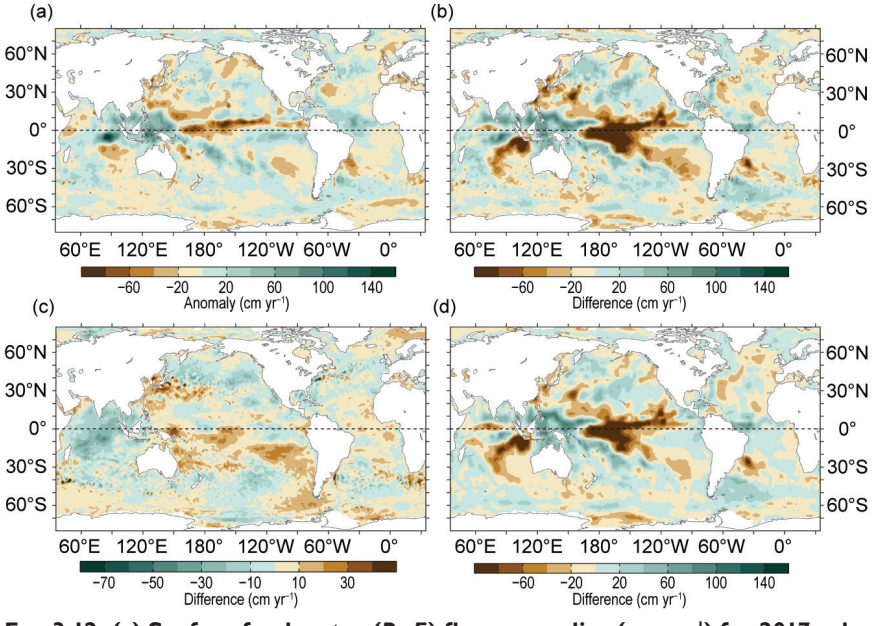

Fig. 3.12. (a) Surface freshwater (*P*–*E*) flux anomalies (cm yr^{-1}) for 2017 relative to a 1988–2014 climatology. 2017 minus 2016 tendencies for (b) *P*–*E*, (c) evaporation (*E*), and (d) precipitation (*P*). Green colors denote anomalous ocean moisture gain and browns denote loss, consistent with the reversal of the color scheme in (c). *P* is computed from the GPCP version 2.3 product, and *E* from OAFlux-HR satellite-based analysis.

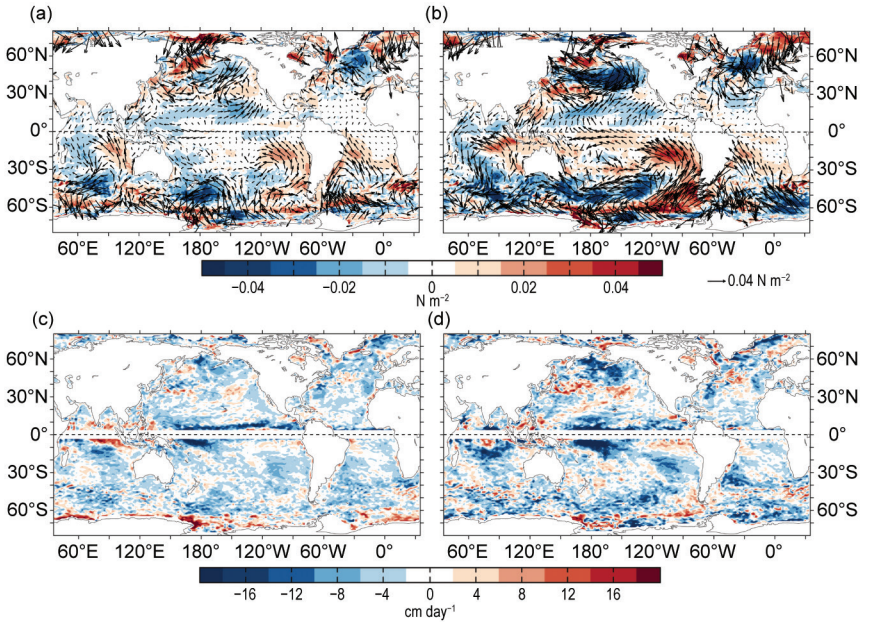

Fig. 3.13. (a) Wind stress magnitude (colors) and vector anomalies (N m^{-2}) for 2017 relative to a 1988–2014 climatology, (b) 2017 minus 2016 differences in wind stress, (c) Ekman vertical velocity (W_{EK}; cm day^{-1}) anomalies for 2017 relative to a 1988–2014 climatology, and (d) 2017 minus 2016 differences in W_{EK}. In (c) and (d), positive values denote upwelling favorable differences, and values are not presented within ±3° of the equator. Winds are computed from the OAFlux-HR satellite-based vector wind analysis.

the ocean by wind stress. Evaporation connects heat and moisture transfers, and the latter, together with precipitation, determines the local surface freshwater flux. Identifying changes in the air–sea fluxes is essential in deciphering observed changes in ocean circulation and its transport of heat and salt from the tropics to the poles.

Air–sea heat flux, freshwater flux, and wind stress in 2017 and their relationships with ocean surface variables are examined here. The net surface heat flux, Q_{net}, is the sum of four terms: SW + LW + LH + SH. The net surface freshwater flux into the ocean (neglecting riverine and glacial fluxes from land) is simply precipitation (P) minus evaporation (E), or the $P-E$ flux. Wind stress is computed from satellite wind retrievals using the bulk parameterization of Edson et al. (2013). The production of the global maps of Q_{net} (Fig. 3.11), $P-E$ (Fig. 3.12), and wind stress (Fig. 3.13) and the long-term perspective of the change of the forcing functions (Fig. 3.14) integrate multigroup efforts. Ocean-surface LH, SH, E, and wind stress are from the Objectively Analyzed air–sea Fluxes (OAFlux; http://oaflux.whoi.edu) project's newly developed satellite-derived, high-resolution (hereafter OAFlux-HR) products (Yu and Jin 2012, 2014, 2018). Surface SW and LW radiative fluxes are from the Clouds and the Earth's Radiant Energy Systems (CERES) Fast Longwave And Shortwave Radiative Fluxes (FLASHFlux; https://ceres.larc.nasa.gov/products.php?product=FLASHFlux) Ed3A product (Stackhouse et al. 2006). Global P is from the Global Precipitation Climatology Project (GPCP; http://gpcp.umd.edu) version 2.3 products (Adler et al. 2003). The CERES Energy Balanced and Filled (EBAF) surface SW and LW version 4.0 products (http://ceres.larc.nasa.gov; Loeb et al. 2018) are used in the time series analysis.

1) Surface heat fluxes

The dominant feature in the 2017 Q_{net} anomalies (Fig. 3.11a) is the broad-scale ocean heat gain anomalies (positive Q_{net}) generally exceeding 10 W m^{-2} in the tropical Pacific and Indian Oceans. The anomaly pattern in the equatorial Pacific is associated with La Niñas at the end of both 2016 and 2017 bracketing neutral conditions in between, so the central and eastern tropical Pacific were cooler than normal both at the beginning and end of 2017. Convection was located more in the far western Pacific and less in the central Pacific, and SSTA was lower in the equatorial central and eastern Pacific (see Fig. 3.1a). The 2017 minus 2016 net downward radiation (SW+LW) differences (Fig. 3.11c) were positive (ocean heat gain) in the central Pacific and negative in the far west. The maximum SW+LW differences were centered near the dateline and extended both to the east along the ITCZ location and to the southeast into the South Pacific. This difference pattern is consistent with the P difference pattern (Fig. 3.12d), showing that SW+LW increased in area of reduced ITCZ rainfall and, conversely, SW+LW reduced in area of increased ITCZ rainfall.

The ocean turbulent heat loss (LH+SH) tendencies from 2016 to 2017 increased (positive anomalies, blue colors) in the equatorial and southeast tropical Pacific (Fig. 3.11d). The enhanced turbulent heat loss tendencies were related primarily to the strengthening tendencies of the southeast trade winds from 2016 to 2017 (Fig. 3.13b). Winds facilitate the efficiency of evaporation; stronger winds usually generate stronger

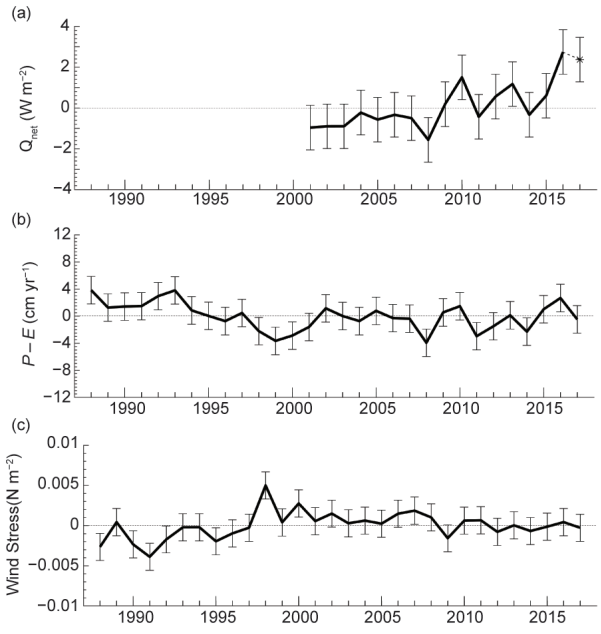

Fig. 3.14. Annual-mean time series of global average anomalies of (a) net surface heat flux (Q_{net}; W m^{-2}) from the combination of CERES EBAF4.0 SW+LW and OAFlux-HR LH+SH, relative to 2000–14. The 2017 Q_{net} (denoted by star) is estimated from FLASHFlux and OAFlux-HR. (b) net freshwater flux ($P-E$; cm yr^{-1}) from the combination of GPCP P and OAFlux-HR E, and (c) wind stress magnitude (N m^{-2}) from OAFlux-HR. Both $P-E$ and wind stress magnitude anomalies are relative to 1988–2014. Gray error bars denote one std. dev. of annual-mean variability.

latent heat loss. In the South Pacific, LH+SH tendencies increased in places where wind speeds strengthened and vice versa. On the other hand, wind is not the only factor controlling LH+SH. The pronounced basin-wide reduction of LH+SH in the tropical Indian Ocean was governed by the basin-wide surface cooling tendencies (see Fig. 3.1b). The surface cooling was also responsible for the reduction of the LH+SH tendencies (by ~10 W m^{-2}) in the North Pacific between 30° and 60°N.

Except for the equatorial Pacific, the 2016 to 2017 Q_{net} tendencies were predominantly determined by LH+SH tendencies. During 2017, the ocean gained more heat in the tropical Indian Ocean, the equatorial Pacific, and the extratropical Pacific and Atlantic between 30° and 60° north and south, while the ocean lost heat in the western Pacific, the south and southeast Pacific, and the subpolar North Atlantic. Net heat loss tendencies south of 60°S may be influenced by sea ice edge effect on flux estimates.

2) Surface freshwater fluxes

The 2017 $P-E$ anomaly pattern is characterized by a reduction of net freshwater input in the central and eastern Pacific and an increase in the Indo-Pacific warm pool (Fig. 3.12a–d). This pattern is primarily in response to the far westward location of tropical convection in association with La Niñas at the ends of both 2016 and 2017. The 2016 to 2017 ITCZ rainfall tendencies (Fig. 3.12d) were reduced considerably in the central equatorial Pacific, with major deficit tendencies (brown) of 1 m and greater centered near the dateline, stretching both eastward and southeastward. At the same time, the far western Pacific and the eastern equatorial Indian Ocean received more rainfall (green) in 2017 than 2016. The pattern reflects the enhanced regional deep convection associated with La Niña. The central tropical Pacific along the ITCZ had a net freshwater deficit by about 0.5 m and the Indo-Pacific warm pool region had a freshwater gain by about 0.3 m relative to climatology (Fig. 3.12a).

The tropical Indian Ocean in 2017 experienced a basin-wide reduction in evaporation, leading to less moisture loss from the region, or equivalently, more freshwater gain (Fig. 3.12c). There were widespread sea surface cooling tendencies, which appear to be a leading factor causing the reduced E tendencies. Wind may contribute too, as the cooling was also accompanied by weakened surface winds in the western Indian Ocean. Away from the Indian Ocean, however, E tendencies were governed mostly by wind tendencies. For instance, the enhanced E tendencies in the tropical and South Pacific were associated with enhanced wind tendencies, and the weakened E tendencies in the North Pacific were associated with weakened wind tendencies. A similar correlation pattern is also observed in the Atlantic basin from 45°S to 75°N. The increase of E in the tropical and subpolar North Atlantic and the reduction of E in both the north and south subtropical basins were primarily the work of wind.

3) Wind stress

The 2017 wind stress anomalies were most pronounced in the extratropical regions (Figs. 3.13a,b). Large negative anomalies were generally associated with the weakening of westerly winds in the midlatitude North Pacific (30°–50°N), the subpolar North Atlantic, and along the Antarctic Circumpolar Current in the Southern Ocean (30°–60°S). In the equatorial region, enhanced deep convection associated with La Niña conditions strengthened the surface branch of the Walker circulation (Rasmusson and Carpenter 1982) from 2016 to 2017, with stronger easterly anomalies in the central equatorial Pacific. Meanwhile, there was a strengthening of the southeast trade winds in the South Pacific and a weakening

of the northeast trade winds in the North Pacific from 2016 to 2017.

Winds vary considerably in space. These spatial variations of winds cause divergence and convergence of the Ekman transport, leading to a vertical velocity, denoted by Ekman pumping (downward) or suction (upward) velocity W_{EK}, at the base of the Ekman layer. Computation of W_{EK} follows the equation: $W_{EK} = 1/\rho\nabla\times(\tau/f)$, where ρ *i*s the density and f the Coriolis force. The 2016 to 2017 W_{EK} tendencies (Fig. 3.13d) reveal stronger downwelling (negative) anomalies in the vicinity of the ITCZ location (3°–5°N) and stronger upwelling (positive) anomalies in the eastern equatorial Indian Ocean. Outside of the tropical region, the weakened westerly band in the midlatitude North Pacific induced a band of upwelling anomalies (positive) to its south and a band of downwelling anomalies (negative) to its north. In the North Atlantic, W_{EK} anomalies were characterized by a tripole pattern, with positive upwelling anomalies at midlatitudes (40°–60°N) and negative downwelling anomalies at subpolar latitudes (poleward 60°N) as well as the subtropical latitudes (5°–30°N). Negative downwelling anomalies dominated the ocean basins in the Southern Hemisphere (Fig. 3.13d).

4) Long-term perspective

Annual-mean time series of Q_{net}, $P-E$, and wind stress anomalies averaged over the global ice-free oceans (Figs. 3.14a–c) provide a decadal perspective on the ocean surface forcing functions in 2017. The Q_{net} time series from 2001 to 2016 were constructed from the CERES EBAF4.0 surface radiation and OAFlux-HR turbulent heat fluxes, and the Q_{net} in 2017 was diagnosed from FLASHFlux and OAFlux-HR. Q_{net} forcing functions were down slightly in 2017.

Recalling that the ocean has absorbed heat at an average rate of about 0.7 W m^{-2} from 1993 through 2017 (see Section 3c), the time series of Q_{net} anomalies indicate that the heat budget over the global ocean displays contrasting patterns before and after 2008. Q_{net} was relatively constant from 2001 to 2007, but after a sharp increase from 2008 to 2010, Q_{net} became more volatile on interannual time scales. The time series of $P-E$ anomalies and wind stress anomalies are about 30 years long, starting from 1988 when Special Sensor Microwave Imager observations became available. Over the 30-year period, $P-E$ experienced a slight decrease during the 1990s but had no obvious trend in the 2000s. The $P-E$ dip in 2008 coincided well with that of Q_{net}, suggesting a coherence between $P-E$ and Q_{net} over the global ocean. A strengthening of the global winds in the 1990s is observed, followed by a period of no trend in the 2000s. The time series showed also a dip in 2009, lagging behind Q_{net} and $P-E$ by one year, and the mean level of the global winds was slightly lower thereafter.

f. Sea level variability and change—P. R. Thompson, M. A. Merrifield, E. Leuliette, W. Sweet, D. P. Chambers, B. D. Hamlington, S. Jevrejeva, J. J. Marra, G. T. Mitchum, R. S. Nerem, and M. J. Widlansky

Global mean sea level (GMSL) during 2017 became the highest annual average in the satellite altimetry record (1993–present), rising to 77 mm above the 1993 average (Fig. 3.15a). This marks the sixth consecutive year (and 22nd out of the last 24) that GMSL increased relative to the previous year. The new high reflects the ongoing multidecadal trend in GMSL during the satellite altimetry era, 3.1 (±0.2) mm yr^{-1} (Fig. 3.15a), which continues unabated despite relaxing to neutral to weak La Niña conditions following the 2015/16 El Niño (see Section 4b).

An early section of the GMSL time series from satellite altimetry (1993–99) was updated during 2017 to reflect a reevaluation of an algorithm designed to detect drift in the altimeter measurements due to thermal or other changes in the internal hardware of the instrument (Beckley et al. 2017). Applying this correction lowers the global mean rate of change over the altimeter record by 0.3 mm yr^{-1} and increases quadratic acceleration (i.e., two times the quadratic coefficient in a second-order polynomial fit) to 0.1 (±0.04) mm yr^{-2}. When effects of the Pinatubo volcanic eruption and ENSO are subtracted from GMSL variability, the estimated climate-change-driven acceleration in GMSL over the altimeter record is 0.084 (±0.025) mm yr^{-2} (Nerem et al. 2018).

Variations in GMSL (Fig. 3.15a) result from changes in both the mass and density of the global ocean (Leuliette and Willis 2011; Chambers et al. 2017). From 2005 to present, increasing global ocean mass observed by the NASA Gravity Recovery and Climate Experiment (GRACE) accounted for approximately two thirds of the GMSL trend, 2.5 (±0.4) mm yr^{-1}. The positive trend in ocean mass primarily resulted from melting of glaciers and ice sheets (see Sections 2c, 5e, and 5f), but these contributions from land ice were partially offset by increased hydrological storage of fresh water on land, accounting for −0.7 (±0.2) mm yr^{-1} (Reager et al. 2016) of sea level change. Steric (i.e., density-related) sea level rise of 1.3 (±0.2) mm yr^{-1}, as observed by the Argo profiling float array, is mostly owing to ocean warming and accounts for the balance of the GMSL trend since 2005.

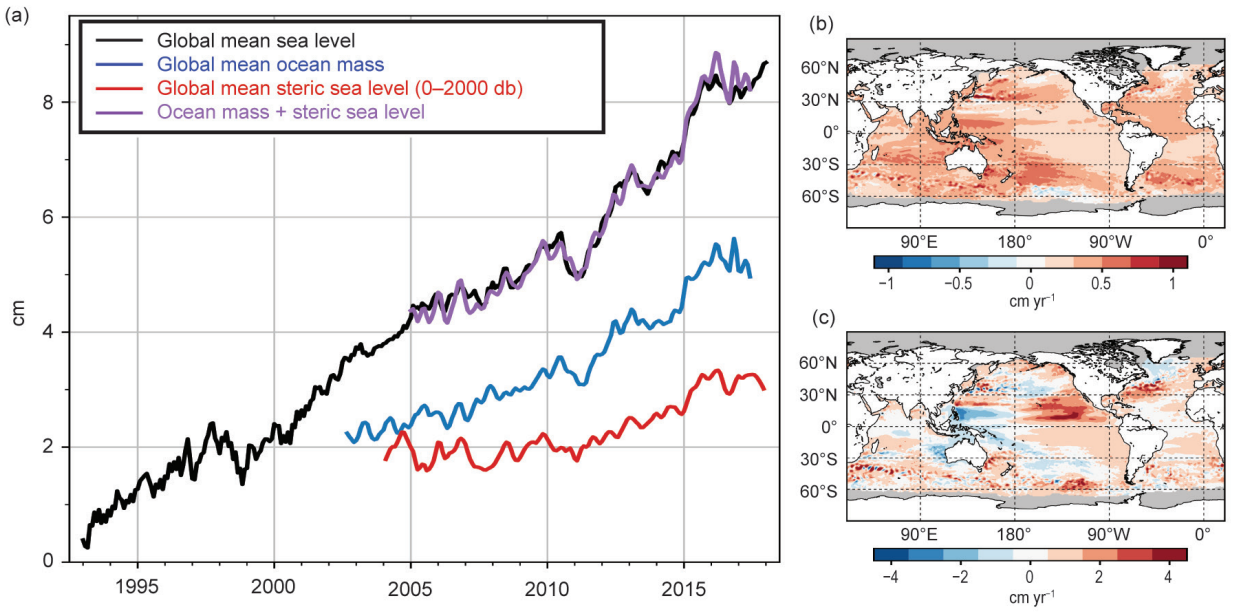

Fig. 3.15. (a) Monthly averaged global mean sea level (cm; black line) observed by satellite altimeters (1993–2017) from the NOAA Laboratory for Satellite Altimetry relative to the start of the altimeter time series in late 1992. Monthly averaged global ocean mass (blue line; 2003–Aug 2017) from GRACE. Monthly averaged global mean steric sea level (red line; 2004–17) from the Argo profiling float array. Mass plus steric (purple line). All time series have been smoothed with a 3-month filter. (b) Linear sea level trends (cm yr^{-1}) from altimetry during 1993–2017. (c) Linear sea level trends (cm yr^{-1}) from altimetry during 2012–17.

GMSL from altimetry observations increased from 2016 to 2017 by 0.9 mm (Fig. 3.15a). A majority of this moderate increase resulted from warming of the upper 400 m of the global ocean (see Fig. 3.5) and a 0.6 mm increase in global mean steric sea level observed by Argo (Fig. 3.15a). Unfortunately, the mass contribution to the year-over-year increase cannot be directly ascertained due to failure of an accelerometer on board one of the GRACE satellites, which resulted in only five months of valid GRACE observations during 2017 (January and March–June). Global ocean mass averaged over these five months of data (after removing the mean seasonal variability) decreased relative to the 2016 average equivalent to 4.8 (±2.4) mm in sea level change, where the uncertainty represents one standard error accounting for the different number of data points in the 2016 and 2017 averages and the substantial monthly uncertainties in the 2017 data (Fig. 3.15a). Closing the sea level budget requires a small (~0.3 mm) sea level equivalent for year-over-year increase in global ocean mass. Thus we can infer an approximate increase in global ocean mass equal to roughly 5 mm of sea level rise over the second half of 2017 to recover mass lost from the ocean early in the year.

Regional sea level trends can differ substantially from the global mean trend, but as the altimetry record has grown in length—capturing complete cycles of decadal oscillations in the process—the long-term trend map has become more uniform (Fig. 3.15b). During the altimetry era, rates of sea level change in the Indian Ocean and western tropical Pacific (3 to 7 mm yr^{-1}) generally exceed the global average rate while rates in the eastern Pacific (1 to 3 mm yr^{-1}) are below the global mean. East–west trend differences across the Pacific result from fluctuations in trade winds, which strengthened during a multidecadal trend toward the La Niña-like phase of the PDO during the first 15–20 years of the satellite record (e.g., Merrifield 2011). More recently, a trend toward El Niño-like conditions during 2012–17 resulted in a reversal of the Pacific zonal trend pattern (Hamlington et al. 2016) with a majority of the eastern Pacific experiencing rates of sea level rise greater than 10 mm yr^{-1} (Fig. 3.15c). Over the same period, positive sea level trends in the North Atlantic subtropical gyre opposed negative sea level trends in the subpolar gyre (Fig. 3.15c). The recent North Atlantic trends suggest increasing gyre strength, which is coincident with a positive trend in the North Atlantic Oscillation (NAO). The tendency toward a positive NAO state in recent years represents a reversal of decadal trends in the Atlantic observed in leading modes of wind-stress curl over the basin throughout the 1990s and 2000s (Häkkinen et al. 2013).

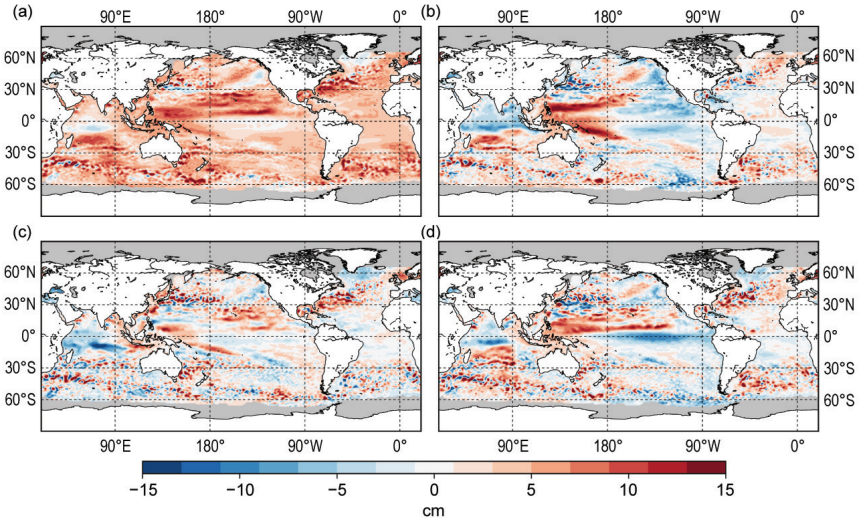

Fig. 3.16. (a) Annual average sea level anomaly during 2017 relative to the average sea level at each location during 1993–2017. (b) Average 2017 sea level anomaly minus 2016. (c) Average sea level anomaly during Dec 2016–Feb 2017 (DJF) relative to the DJF average during 1993–2017. (d) Same as (c), but for Sep–Nov 2017. GMSL was subtracted from (c) and (d) to emphasize regional, non-secular change. Altimetry data were obtained from the gridded, multimission product maintained by the Copernicus Marine and Environment Monitoring Service (CMEMS).

Positive annual sea level anomalies spanned most of the global ocean during 2017 (Fig. 3.16a), which primarily reflects the global mean trend relative to the 1993–2017 climatology. The change in annual mean sea level from 2016 to 2017 (Fig. 3.16b; similar to OHC, see Fig. 3.4b) shows an increase in the western tropical Pacific and decrease in the eastern tropical Pacific. This zonal pattern is consistent with the continuation of ENSO-neutral to weak La Niña conditions during most of 2017 in contrast to 2016, which began in a strong El Niño state. Despite decreased trade wind strength over the North Pacific from 2016 to 2017 (see Fig. 3.13b), sea level increased in the western North Pacific due in part to downwelling (i.e., positive sea level) oceanic Rossby waves propagating east to west across the basin during the year (Figs. 3.16c,d). These propagating anomalies were likely reinforced by a tendency toward downwelling Ekman pumping anomalies at low latitudes north of the equator (see Fig. 3.13d). A similar tendency toward downwelling Ekman pumping occurred south of the equator, which likely accounts for the increase in sea level in the western South Pacific.

Tendencies in the Indian Ocean show decreased sea level from 2016 to 2017 across the equatorial and north Indian Ocean (ENIO) while sea levels increased in the south Indian Ocean subtropical gyre region (Fig. 3.16b). The Indian Ocean tendencies are most likely linked to an increase in trade wind strength south of the equator (see Fig. 3.13d) and are consistent with the tendency toward enhanced westward geostrophic surface currents in the region of the Indian Ocean South Equatorial Current (see Fig. 3.18b). Increasing trades in the region create more negative wind-stress curl near the equator, which in turn enhances subtropical and cross-equatorial overturning cells (e.g., Miyama et al. 2003) that can lead to near-uniform variability in sea level across the ENIO (Thompson et al. 2016).

Ongoing trends and year-to-year changes in sea level impact coastal communities by increasing the magnitude and frequency of positive sea level extremes that cause flooding and erosion. In many areas, coastal infrastructure is currently exposed to nuisance-level (i.e., minor-impact) flooding when water levels exceed a threshold defined by the top 1% of observed daily maxima from a global network of tide gauges (Sweet et al. 2014). These thresholds vary geographically (Fig. 3.17a) but are typically around 0.5 m above mean higher high water (MHHW)—the average of observed daily maxima—and are expected to be exceeded 3–4 times per year. Most locations along the U.S. East Coast experienced greater-than-expected numbers of exceedances during 2017 (Fig. 3.17b), due in part to mean sea level trends in the region that exceed the global mean rate at multiple time scales (Figs. 3.15b,c). The number of events over most of the U.S. East Coast in 2017 decreased relative to 2016 (Fig. 3.17c), however, as mean sea levels decreased year-over-year in the western North Atlantic (Fig. 3.16b). Year-over-year increases in threshold exceedances occurred across the tropical North Pacific and along the western coast of South America (Fig. 3.17c). The increase in the North Pacific, including Hawaii (see Sidebar 3.2), is at least partially related to the positive sea level anomalies propagating across the region during 2017 (Figs. 3.16c,d). In contrast, increased exceedances along the western coast of South America cannot be readily attributed to mean sea level change, as neither trends nor annual sea level anomalies are anomalous in the region.

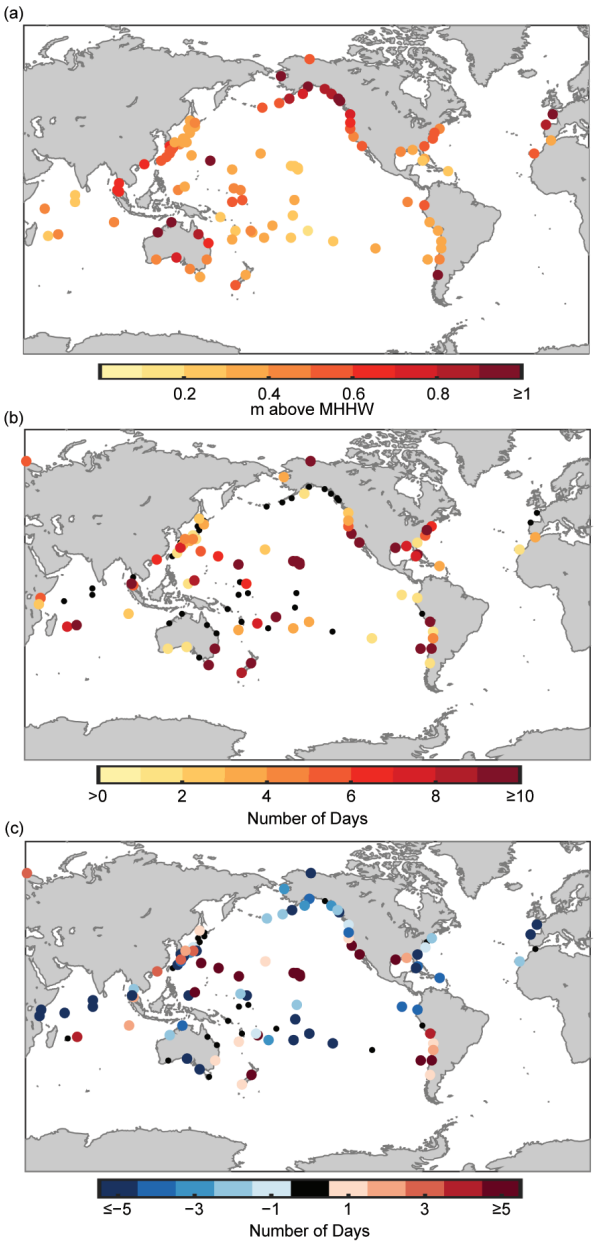

Fig. 3.17. (a) Nuisance-level flooding thresholds defined by the level of the top 1% of observed daily maxima during 1998–2016 from tide gauge records. Units are in meters above mean higher high water (MHHW) calculated over 1998–2016. (b) Number of daily maximum water levels during 2017 above the thresholds in (a). Small, black circles in (b) and (c) indicate a value of zero. (c) Same as in (b), but for 2017 minus 2016. Daily maximum water levels were calculated from hourly tide gauge observations obtained from the University of Hawaii Sea Level Center Fast Delivery database. Only records with at least 80% completeness during 1996–2016 and 80% completeness during 2017 were analyzed.

g. Surface currents—R. Lumpkin, G. Goni, and K. Dohan

This section describes ocean surface current changes, transports derived from ocean surface currents, and features such as rings inferred from surface currents. Surface currents are obtained from in situ (global array of drogued drifters and moorings) and satellite (altimetry, wind stress, and SST) observations. Transports are derived from a combination of sea height anomaly (from altimetry) and climatological hydrography. See the *State of the Climate in 2011* report for details of these calculations. Zonal surface current anomalies are calculated with respect to a 1992–2007 climatology and are discussed below for individual ocean basins.

1) Pacific Ocean

In 2017, the Pacific basin exhibited annual mean zonal westward current anomalies of 5–20 cm s^{-1} at 1°–7°N across much of the basin (Fig. 3.18a), with peak values of 20 cm s^{-1} at 6°N, 125°–145°W. This anomaly had two proximate causes: a northward shift of the North Equatorial Countercurrent (NECC), normally centered on 7°N but in 2017 on 8°N; and a strengthened northern South Equatorial Current (nSEC) at 2°N, which is 50 cm s^{-1} westward in the annual climatology but averaged 60 cm s^{-1} in

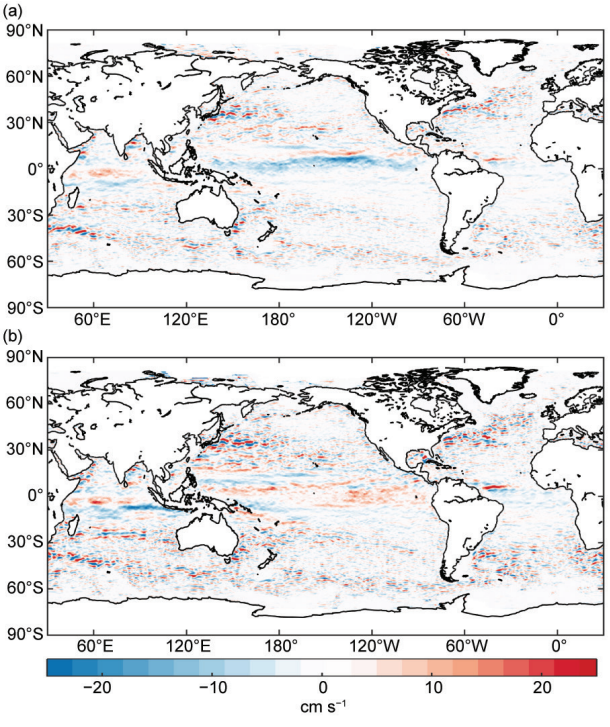

Fig. 3.18. Annually averaged geostrophic zonal surface current anomalies (cm s^{-1}) for (a) 2017 relative to a 1992–2007 climatology and (b) 2017 minus 2016 zonal currents (cm s^{-1}) derived from a synthesis of drifters, altimetry, and winds.

SIDEBAR 3.2: NU'A KAI: FLOODING IN HAWAII CAUSED BY A "STACK" OF OCEANOGRAPHIC PROCESSES—H. YOON, M. J. WIDLANSKY, AND P. R. THOMPSON

The Hawaiian Islands experienced record-high sea levels during 2017 (Fig. SB3.3; also see Fig. 3.17b), which caused nuisance flooding in vulnerable coastal communities and exacerbated beach erosion, especially around times of highest tides. During April and May, tide gauges throughout the main Hawaiian Islands recorded water levels that were 20–30 cm above the astronomical tidal predictions (levels expected based only on the Earth–Moon–Sun's gravitational pull upon the ocean). On 21 August 2017, the tide gauge in Honolulu Harbor observed the highest hourly water level, 99 cm above mean lower low water (MLLW), since records began in 1905. In addition to this new maximum, the gauge registered an unprecedented number of high-water events. In the 112-year record, sea level in Honolulu Harbor exceeded 90 cm above MLLW—the approximate level of nuisance flooding—on just 40 days; 15 of those days occurred during 2017. The highest observed water levels generally occurred under clear skies with wind and rain playing little to no role in the flooding impacts.

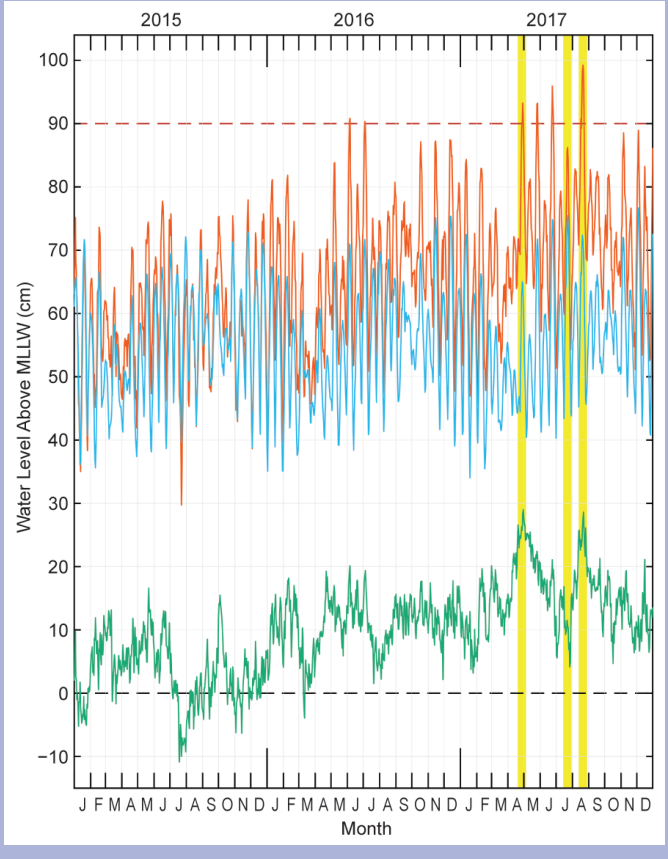

FIG. SB3.3. Daily maximum hourly sea levels (cm) for Honolulu, HI. Tide predictions (blue) are based on harmonic analysis of the Honolulu Harbor sea level recorded during the NTDE (1983–2001). Predictions and observations (orange) are with respect to the MLLW datum. Residuals between the observed sea levels and the tide prediction are shown by the green line. For reference, the 90-cm water level is shown (dashed horizontal line), which is a threshold for coastal impacts near Honolulu.

The repeated flooding events on fair-weather days during 2017 generated substantial scientific and media interest. Near-real-time analyses of tide gauge observations and satellite-based altimetry measurements of sea surface heights around Hawaii allowed the above-normal sea levels to be broken down into five primary contributions: 1) long-term sea level rise, 2) seasonally high astronomical tides, 3) oceanic planetary waves, 4) oceanic mesoscale eddies, and 5) an inverse-barometer effect of low atmospheric pressure on the ocean. This combination of processes contributing to high sea levels in Hawaii has become known as Nu'a Kai, which means "piled ocean" in the Hawaiian language and helps to convey the sense of multiple components of sea level variability stacking together to produce tangible impacts at the coast.

Any one component of Nu'a Kai would not have caused extreme high sea levels on its own. Long-term sea level rise relative to the National Tidal Datum Epoch (NTDE; 1983–2001), on which tidal datums are based, is approximately 4 cm near Hawaii. However, sea level rose during the 20th century more than 12 cm prior to the current NTDE, and none of the 2017 events would have reached nuisance-flood levels without this long-term trend. Large-scale (> 500 km in zonal width) anomalies raised background sea level around the Hawaiian Islands during most of 2017 (see Figs. 3.16c,d), including 13 and 16 cm above normal during

2017. Because 2016 on average had similar westward anomalies over a broader area, the 2017 minus 2016 tendencies (Fig. 3.18b) do not show this feature but instead exhibit narrow bands of eastward anomaly differences. The northward shift of the NECC also produced eastward anomalies of ~10 cm s^{-1} at 8°–12°N. On the equator, eastward anomalies of 10–15 cm s^{-1} were at 0°–1°S, associated with the presence of a ~10 cm s^{-1} equatorial surface countercurrent not present in the 1992–2007 climatology.

From the start of 2017, all of the major anomalies present in the annual average anomaly map were

the highest water level events of April and August, respectively (highlighted in Fig. SB3.3). These anomalies were associated with an oceanic Rossby (planetary) wave, which propagated slowly westward across the tropical North Pacific over the past year. In addition, a series of energetic mesoscale eddies impinged on Hawaii, either elevating or lowering sea levels depending on whether they were anti-cyclonic or cyclonic. Anti-cyclonic eddies near Honolulu during flood events in April and August raised sea levels by 10 and 5 cm, respectively (Fig. SB3.4). Low atmospheric pressure made additional, non-negligible contributions to Nu'a Kai via the inverse-barometer effect during April and August, increasing water levels by an additional 4 and 2 cm. In total, the sum of all non-tidal components of the highest levels during April and August was close to 30 cm above MLLW, but the relative contributions of each component differed in each case.

The coastal impacts of the non-tidal contributions to Nu'a Kai described above (e.g., overwash and erosion of the famed Waikiki Beach) occurred during seasonally large astronomical high tides, which contributed another 7 and 16 cm above the average tidal range in April and August, respectively. Astronomical tides are a necessary component of Nu'a Kai, but the highest sea levels of 2017 did not occur during the month with the highest high tides of the summer (July; Fig. SB3.3). During the highest tides of July, a cyclonic eddy near Honolulu lowered sea level by 6 cm (Fig. SB3.4), which cancelled much of the large-scale contribution to Nu'a Kai (the inverse-barometer effect was negligible). As a result, at no time during July did the Honolulu tide gauge record water levels above 90 cm and no significant coastal impacts occurred, unlike during April and August when astronomical tide cycles were less extreme.

There is a pressing need to understand the causes and implications of the unprecedented number of high sea level events across Hawaii during 2017, because increasing global mean sea level rise will increase the frequency of such periods of coastal flooding in the future (see Fig. 3.15a). Whereas the magnitude of each component of Nu'a Kai can be reasonably well-quantified in hindsight, a number of questions remain concerning the forcing, duration, and probability of reoccurrence. Most importantly, the largest non-tidal components of Nu'a Kai are oceanic Rossby waves and mesoscale eddies. Eddies can be difficult to predict, which makes it challenging for those affected by Nu'a Kai to prepare for the events. Researchers at the University of Hawaii are working toward high sea level forecast products, which will be improved by more complete dynamical understanding. By the end of 2017, Honolulu sea level anomalies decreased relative to earlier in the year, but levels remained above normal.

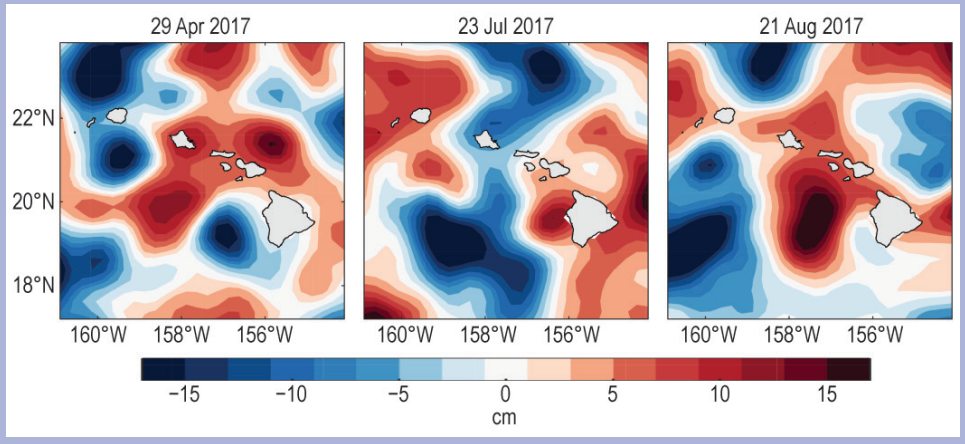

Fig. SB3.4. Daily mean sea surface height anomalies (cm) from satellite altimetry (CMEMS/AVISO). The spatial mean has been removed over the domain of each map to highlight mesoscale structure.

already established. The evolution of these features through the year (Fig. 3.19) was as follows:

Eastward anomalies of 20–33 cm s^{-1} were present in the central and eastern equatorial Pacific in January 2017, with peak values at 0°–1°S, 115°–155°W, associated with the anomalous surface equatorial countercurrent. These anomalies intensified in February to maximum values of 40 cm s^{-1} and persisted through March. While the countercurrent did not weaken significantly in April, anomalies were weaker because the climatological flow reverses to eastward at these latitudes in April. This situation was main-

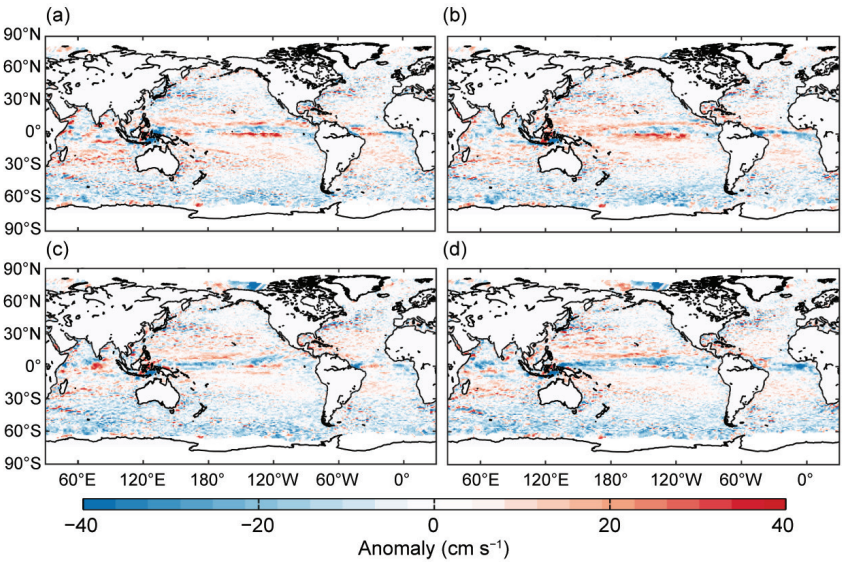

Fig. 3.19. Seasonally averaged zonal geostrophic surface current anomalies (cm s^{-1}) with respect to a 1992–2007 seasonal climatology, for (a) Dec 2016–Feb 2017, (b) Mar–May 2017, (c) Jun–Aug 2017, and (d) Sep–Nov 2017.

tained through June. In July, when the climatological equatorial current reverses again to westward, the flow was near zero (an eastward anomaly of 5–10 cm s^{-1}). By August, the equatorial current was westward (no longer a countercurrent) and remained close to climatology for the remainder of the year.

The northward shift of the NECC was already present in January 2017. By March, core speeds of the NECC were a maximum of 25–30 cm s^{-1} at 8°N, compared to 20 cm s^{-1} at 7°N in the March climatology. Eastward velocity associated with the NECC extended north to 11°N, compared to 9.5°N in climatology. Anomalies with respect to the April climatology were dramatic, as the NECC maintained its intensity through the month when it weakens in climatology. However, the NECC then rapidly weakened, becoming anomalously weak (westward anomalies of ~5 cm s^{-1}) in May. For the remainder of the year, the NECC was close to its climatological strength, with a core latitude also matching climatology in June–August and a shift to the north with respect to climatology in September–December.

In all months of 2017, the northern branch of the SEC was faster to the west than in climatology, with little seasonal variation in the magnitude of this anomaly as the current followed typical seasonal variations, weakening from March to May and strengthening from June to October.

As noted in earlier *State of the Climate* reports (e.g., Dohan et al. 2015), the Kuroshio was shifted anomalously northward in 2010–14, although this shift diminished during 2014. During 2015 through 2017, the Kuroshio has remained close to its climatological latitude. These shifts reflect a decadal stable/unstable oscillation of the Kuroshio jet (Qiu and Chen 2005), which shifts to the north when it intensifies and becomes stable, thus lowering eddy kinetic energy (EKE). Averaged in the downstream Kuroshio jet region 32°–38°N 141°–153°E, (Qiu and Chen 2005) EKE was low in 1994/95, elevated in 1999–2001, low in 2002/03, reached a peak in 2005, and then decreased from 2009 to 2015. Since 2015, EKE has remained relatively steady (at interannual time scales) and somewhat lower than the 1993–2017 average in the downstream Kuroshio jet region, while exhibiting intra-annual variations such as a short-lived increase in mid-2016. During 2017, EKE in the region averaged 0.10 m^2 s^{-2} compared to the 1993–2017 average of 0.18 m^2 s^{-2}.

Changes in the equatorial Pacific current system that advect surface waters across the basin result in anomalies in the SST fields. The behavior of the surface current anomalies in this region is an indicator of upcoming SST anomalies with surface current anomaly behavior leading SST anomalies by several months. This leading nature can be seen in the first

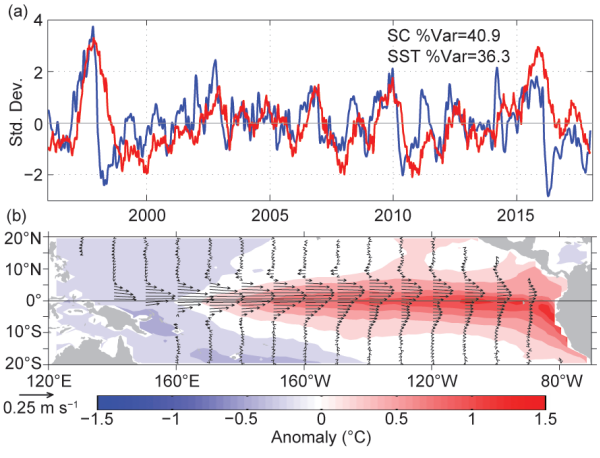

Fig. 3.20. Principal EOF of surface current (SC; m s^{-1}) and of SST anomaly (°C) variations in the tropical Pacific from the OSCAR model (Bonjean and Lagerloef 2002; www.esr.org/enso_index.html). (a) Amplitude time series of the EOFs normalized by their respective std. dev. (b) Spatial structures of the EOFs.

principal empirical orthogonal function (EOF) of surface current (SC) anomaly and separately the first EOF of SST anomaly in the tropical Pacific basin (Fig. 3.20). The maximum correlation between SC and SST anomalies is R = 0.65 for 1993–2017, with SC leading SST anomalies by 76 days. The year 2017 began with a continued lessening of the dramatic negative SC anomalies of 2016, approaching zero values in January. Although the EOF amplitude for SC anomalies was negative throughout 2017, this lessening coincided with an increase in positive SST anomalies, with a maximum SST EOF amplitude in March of 0.9 standard deviations. As the year progressed the SC EOF amplitude decreased to a minimum of –1.9 standard deviations in October. The SST EOF followed this trend with a steady decrease after the peak in March to a minimum of –1.2 standard deviations in December. The year ended with SC anomalies again approaching zero.

2) Indian Ocean

The annually averaged near-equatorial current in the Indian Ocean basin is eastward, reflecting the dominance of the Southwest Monsoon Current in the annual average. During 2017, the mean current near the equator had peak values of 33–35 cm s^{-1}, somewhat elevated from its climatological average of 25–27 cm s^{-1} (Fig. 3.18a). Because these anomalies were much stronger in 2017 than in 2016, the 2017 minus 2016 tendencies (Fig. 3.18b) are negative on the equator. An examination of the month-by-month development of these anomalies reveal that they reflect a much stronger-than-average Southwest Monsoon Current during July–October 2017. Maximum eastward anomalies of 30–35 cm s^{-1} were observed at 1°–2°S, 65°–85°E, in August.

3) Atlantic Ocean

Annual mean anomalies in the Atlantic Ocean (Fig. 3.18a) indicate an ~15 cm s^{-1} strengthening of the eastward NECC at 5°–6°N, 33°–50°W and a 20–25 cm s^{-1} strengthening of the westward nSEC at 0°–1°N, 25°W–0°. The year began with the NECC anomaly established but with an anomalously weak (by 5–10 cm s^{-1}) nSEC (Fig. 3.19). In February, strengthening of the nSEC had developed east of 24°W and spanned the basin in March. These anomalies weakened through April and May, and in June–August the nSEC was close to climatology. Westward anomalies again developed in the nSEC in September and persisted through November. In December, the nSEC was close to its climatological December strength.

The changes in transport and location of several key surface currents and mesoscale rings associated with them in the Atlantic Ocean basin are continuously monitored using satellite altimetry observations (www.aoml.noaa.gov/phod/altimetry/cvar/index.php). During 2017, the number of rings shed by the Agulhas and North Brazil Currents, which are partly indicative of Indian–Atlantic and South–North Atlantic water mass exchanges, respectively, remained within their mean 1993–2017 values. The altimetry-derived transports of the Agulhas, Malvinas, Brazil, North Brazil, and Florida Currents did not exhibit 2017 variations beyond one standard deviation from their mean 1993–2017 values. In the southwest Atlantic Ocean, the separation of the Brazil Current from the continental shelf break (located at 37.6°S in the mean) reveals the intrusion of subtropical waters into the subpolar region. Since 1993, this current has separated farther to the south from the continental shelf break by 3° latitude (c.f., Lumpkin and Garzoli 2011; Goni et al. 2011). Compared to its mean value in 2016, the separation moved to the south by about 2° latitude (see www.aoml.noaa.gov/phod/altimetry/cvar/mal/BM_ts.php), the largest southward shift in the altimeter time period 1993–present.

h. Meridional overturning and oceanic heat transport circulation observations in the North Atlantic Ocean—M. O. Baringer, J. Willis, D. A. Smeed, B. Moat, S. Dong, W. R. Hobbs, D. Rayner, W. E. Johns, G. Goni, M. Lankhorst, and U. Send

The Atlantic meridional overturning circulation (AMOC) and the Atlantic meridional heat transport (AMHT) carry warm near-surface water northward, provide heat to the atmosphere at northern latitudes, and carry colder deep water southward. Buckley and Marshall (2016) present a summary of the dynamical forcing mechanisms of the AMOC and AMHT and the role they play in regulating climate variability around the Atlantic sector. Owing to the large amounts of heat, carbon, and fresh water transported by the AMOC, climate models suggest accurate estimation of its rate of change is critical to understanding and predicting our changing climate (e.g., W. Liu et al. 2017; Rahmstorf et al. 2015). Even on short time scales the AMOC/AMHT can impact climate (e.g., Duchez et al. 2016). These recognitions have led to the implementation of enhanced observing systems of the strength of the AMOC in the subpolar North Atlantic (Lozier et al. 2017) and the subtropical South Atlantic (Ansorge et al. 2014). These new observing systems will eventually provide a more complete spatial picture of the state of the AMOC.

In general, estimating the AMOC/AMHT amounts to summing ocean-spanning measurements of the velocity/heat transport horizontally and vertically over the full water column. As all relevant time and space scales cannot be simultaneously measured, all the current AMOC/AMHT time series estimates include trade-offs between one quantity and another and can have errors and biases that are dependent on observing system design (e.g., Sinha et al. 2018). The systems described herein include the AMOC/AMHT observing systems at 41°N, 26°N, and 16°N and AMHT at 41°N, 26°N, and 35°S, which represent the most complete, longest time AMOC/AMHT series currently available.

Studies have shown that density anomalies along the western boundary in particular are essential predictors of the strength of the AMOC (e.g., Le Bras et al. 2017; Yashayaev and Loder 2016), and subpolar density anomalies precede those in the subtropical gyre by 8–10 years; hence, observing systems that measure western boundary variability are particularly essential. The Florida Current (FC; as the Gulf Stream is called at 26°N) observing system is one such example that can provide a longer time perspective of possible AMOC variations (e.g., Frajka-Williams 2015). Providing data since 1982, this is the longest open ocean transport time series (Fig. 3.21). Additionally, FC and AMOC transport variations at all time scales are inversely linked to sea level variations along the east coast (e.g., Domingues et al. 2016). The median FC transport from the full record (1982–2017) is 31.9 (±0.25) Sv (one standard error of the mean assuming a 20-day integral time scale) with a small downward trend of −0.29 (±0.23) Sv decade^{-1} (errors estimating 95% significance as above). The 2017 median FC transport was 32.3 (±1.6) Sv, slightly above the long-term average and the 2016 annual average. Daily FC transports compared to those of all previous years (Fig. 3.21a) indicate that 2017, unlike previous years, had few unusual transport anomalies (extremes defined as outside the 95% confidence limits for daily values). During 2017 there were no high transport events and the only low transport anomaly that was sustained for more than a day occurred during 10–11 December 2017 (averaging 23.6 Sv). The FC lagged by 8 years has its maximum positive correlation with the NAO (Fig. 3.21b). The FC lagged by 5 years has its maximum negative correlation with the Atlantic multidecadal oscillation (AMO). It continues to be inversely correlated with the difference between observed and astronomically predicted sea level at the Lake Worth tide gauge station (Fig 3.21a, significant at over the 99% significance level, correlation coefficient −0.57 and 28% of variance explained).

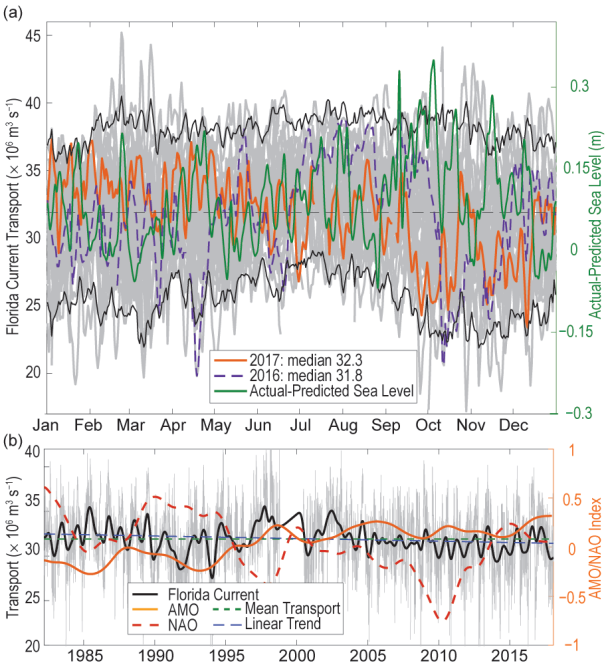

Fig. 3.21. (a) Daily estimates of FC transport (× 10^6 m^3 s^{-1}) during 2017 (orange solid line), 2016 (dashed purple line), and 1982–2015 (light gray lines) with 95% confidence interval of daily transport values computed from all years (black solid line) and the long-term mean (dashed black line). Actual sea level minus predicted sea level at the Lake Worth tide gauge station (dark green line). (b) Daily estimates of FC transport (× 10^6 m^3 s^{-1}) for the full time series record (light gray), smoothed using a 12-month second-order Butterworth filter (heavy black line), mean transport for the full record (dashed black line), and linear trend from 1982 through 2017 (dashed blue line). Two-year low-passed AMO (orange line) and NAO (red dashed line) indices are also shown.

The FC time series contributes to the estimate of the AMOC at 26°N (Figs. 3.22, 3.23), where the AMOC is measured with full-water column moorings that span the full basin and include direct transport measurements in the boundary currents as part of the large RAPID-MOC/MOCHA/WBTS 26°N mooring array (Smeed et al. 2017). The data from these moorings are collected every 18 months, with AMOC data presented in this section extending from April 2004 to February 2017. In the latest update, adding data from October 2015 through February 2017, the AMOC has increased slightly with average AMOC of 17.2 Sv in 2016 and 17 Sv in part of 2017. This seeming stabilization of the downward trend in the AMOC has resulted in a statistically insignificant downward trend estimate of –1.99 (±2.01) Sv decade^{-1}, half the −5.3 Sv decade^{-1} trend first noted in Smeed et al. (2014). This trend is entirely due to the increase

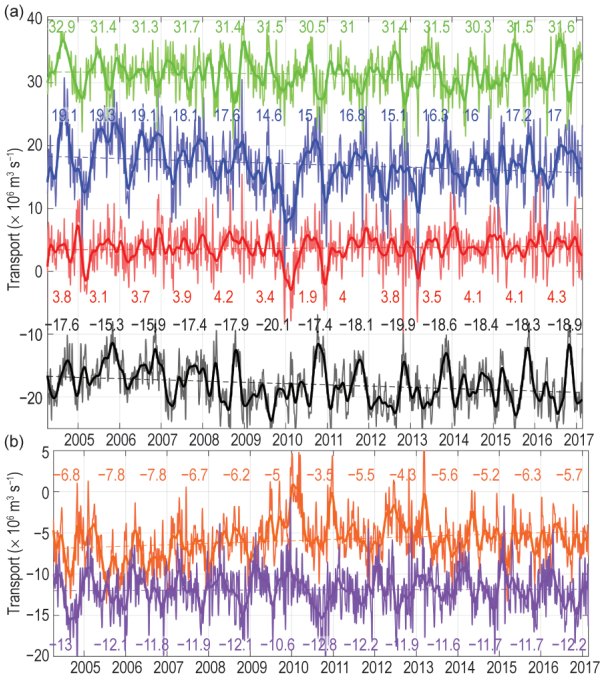

Fig. 3.22. (a) Daily estimates of the volume transport (× 10⁶ m³ s⁻¹) of the meridional overturning circulation (blue line) and its components, the FC (green line), wind-driven Ekman transport (red line), and the geostrophic interior (black line), as measured by the UK National Environmental Research Council (NERC) Rapid Climate Change Program (RAPID-WATCH), the National Science Foundation's Meridional Overturning and Heat transport Array proposal, and the NOAA Western Boundary Time Series project (WBTS). The volume transports have a 10-day low-pass filter applied to the daily values and the annual median transports for each year are shown in the associated color text (Sv). (b) The deepest part of the MOC can be divided into upper deep water (1000–3000 m; orange) and lower deep water (3000–5000 m; purple) transports (× 10⁶ m³ s⁻¹).

in the southward near-surface interior flow of –2.05 (±1.35) Sv decade^{-1} (Fig. 3.22, black dashed line), while the decrease in FC transport balances the increase in Ekman transport. The decrease in the AMOC at this latitude can be explained by the decreased export, 1.65 (±1.07) Sv decade^{-1}, of upper North Atlantic Deep Water in the 1–3 km depth range, while the lowest layer remains fairly stable. Change-point analysis shows that the AMOC time series trend is not linear but rather consists of a significant break or jump in the time series in 2008 (Smeed et al. 2018), and the baseline shift toward decreased AMOC was concurrent with changes of a southward shifting Gulf Stream and large-scale changes of sea surface temperature, sea surface height, and heat content.

AMOC estimates are also provided at 41°N, where a combination of profiling Argo floats (that measure ocean temperature and salinity for the upper 2000 m on broad spatial scales, as well as velocity at 1000 m) and altimetry-derived surface velocity (Willis 2010; Hobbs and Willis 2012) are used to estimate the AMOC (Fig. 3.23) and AMHT (not shown). This time series has been updated since last year's report (Baringer et al. 2017), extending from January 2002 to October 2017. Near 16°N, the AMOC is estimated using a mooring array of inverted echo sounders, current meters, and dynamic height moorings (Send et al. 2011) that measure the flow below 1000 m (the southward flowing part of the AMOC "conveyor belt"); hence, the AMOC estimate at this latitude (Fig. 3.23) is a negative number (southward deep flow) to distinguish these observations from the full water column systems. These data have not been updated since last year's report and remain from February 2000 to September 2016. At 35°S in the South Atlantic, the AMOC and AMHT are estimated

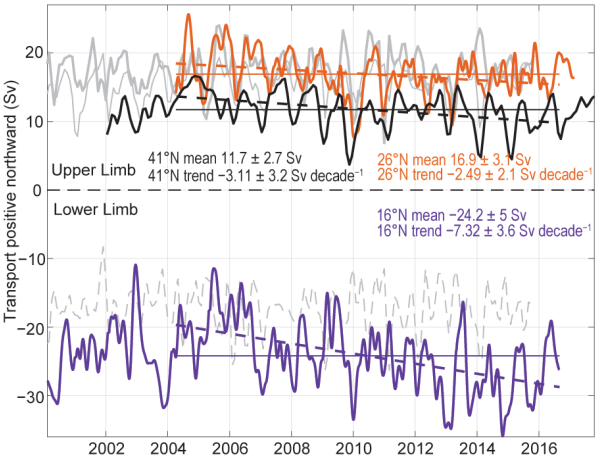

Fig. 3.23. Estimates of AMOC transports (1 Sv = × 10⁶ m³ s⁻¹) from the Argo/Altimetry estimate at 41°N (black; Willis 2010), the RAPID-MOC/MOCHA/WBTS 26°N array (orange; Smeed et al. 2017), and the German/NOAA MOVE array at 16°N (purple; Send et al. 2011) shown vs. year. All time series have a 3-month second-order Butterworth low-pass filter applied. Horizontal lines are mean transports during similar time periods as listed in the corresponding text. Dashed lines are trends for each series over the time period with data available for all three series (Apr 2004 through Aug 2016). For MOVE data, the net zonal and vertical integral of the deep circulation represents the lower limb of the AMOC (with a negative sign indicating southward flow), and hence a stronger negative (southward) flow represents an increase in the AMOC amplitude. Light gray lines show ECCO2-derived transports (Menemenlis et al. 2008): (top) thin gray is the 41°N transport, thick gray is the 26°N transport, (bottom) the negative meridional overturning circulation in the model shown for ease of comparison with the 16°N data.

using a combination of high-density (closely spaced) expendable bathythermograph (XBT) and broader-scale Argo profiling float data (Dong et al. 2014, not shown; www.aoml.noaa.gov/phod/soto/mht/ax18/report.php). These data are collected and analyzed in near-real time, with values spanning July 2002 to September 2017.

Similar to 26°N, at 41°N the AMOC and AMHT are decreasing less rapidly (Fig. 3.23), changing to −0.08 (±2.7) Sv decade^{-1} and −0.03 (±0.04) PW decade^{-1} as compared with −1.2 (±3.0) Sv decade^{-1} and −0.09 (±0.21) PW decade^{-1} reported last year. Farther south, the MOC/MHT trends are positive, but decreasing in the past three years as the annual means at 16°N increased from −29.2 Sv in 2014 to −27.8 Sv in 2015 to −23.8 in 2016. This recent reduction in southward flow has led to a reduced estimate of the long-term trend of the AMOC from February 2000 to September 2016 at 16°N to be +3.4 (±2.4) Sv decade^{-1}. While the 35°S AMOC transport estimate has remained fairly constant for the last three years (median AMOC of about 20 Sv), during 2017 it was dominated by the Ekman component whereas in previous years it had been dominated by the geostrophic component. The variability at all latitudes in the Atlantic is not well correlated and, therefore, data from more than one latitude are needed to describe the state of the ocean.

i. Global ocean phytoplankton—B. A. Franz, E. M. Karaköylü1, D. A. Siegel, and T. K. Westberry

Marine phytoplankton contribute roughly half the net primary production (NPP) on Earth, fixing atmospheric CO_2 into food that fuels global ocean ecosystems and drives biogeochemical cycles (e.g., Field et al. 1998; Falkowski et al. 1998). Phytoplankton growth is dependent on availability of light and nutrients (e.g., iron, nitrogen, phosphorous) in the upper ocean euphotic zone, which in turn is influenced by physical factors such as ocean temperature (e.g., Behrenfeld et al. 2006). SeaWiFS (McClain 2009) and MODIS (Esaias et al. 1998) are satellite ocean color sensors that provide observations of sufficient frequency and geographic coverage to globally monitor changes in the near-surface concentration of the phytoplankton pigment chlorophyll-*a* (Chl*a*; mg m^{-3}), which serves as a proxy for phytoplankton abundance. Here, global Chl*a* distributions for 2017 are evaluated within the context of the 20-year continuous record provided through the combined observations of SeaWiFS (1997–2010) and MODIS on *Aqua* (MODISA, 2002–present). All Chl*a* data used in this analysis correspond to NASA process-

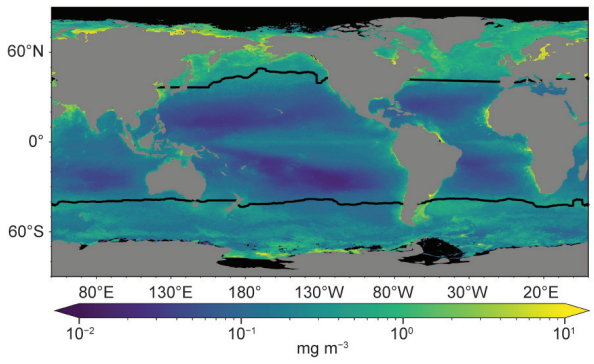

Fig. 3.24. Annual mean Chl*a* distribution mg m^{-3} derived from MODIS on *Aqua* for 2017. Also shown is the location of the mean 15°C SST isotherm (black lines) delineating the boundary of the PSO. Chl*a* data are from NASA Reprocessing version 2018.0. Data are averaged into geo-referenced equal area bins of approximately 4.6 × 4.6 km^2 and mapped to an equirectangular projection centered at 150°W.

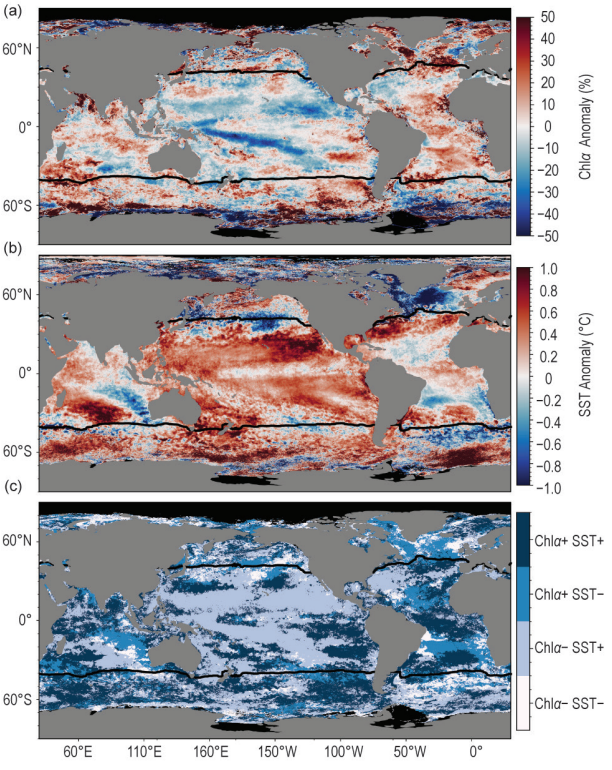

Fig. 3.25. Spatial distribution of average monthly (a) MODISA Chl*a* anomalies and (b) SST anomalies where monthly differences were derived relative to the MODISA 9-year climatological record (2003–11). Chl*a* is expressed as % difference from climatology, while SST is shown as an absolute difference (°C). (c) identifies relationships between the sign of SST and Chl*a* anomalies from panels (a) and (b), with colors differentiating sign pairs and missing data masked in black. Also shown in each panel is the location of the mean 15°C SST isotherm (black lines) delineating the PSO.

ing version R2018.0 (https://oceancolor.gsfc.nasa.gov/reprocessing/), which utilizes common algorithms and calibration methods to maximize consistency in the multi-mission satellite record.

The spatial distribution of MODISA annual mean Chl*a* for 2017 (Fig. 3.24) is consistent with the well-established, physically driven distribution of nutrients (Siegel et al. 2013) and surface mixed-layer light conditions (Behrenfeld et al. 2016). Chl*a* values during 2017 ranged over three orders of magnitude, from < 0.02 mg m^{-3} in the central ocean gyres to > 20 mg m^{-3} in nutrient-rich coastal and subpolar waters. To assess changes in this distribution during 2017, mean values for MODISA Chl*a* in each month of the year were subtracted from monthly climatological means for MODISA (2003–11). These monthly fields were then averaged to produce the global chlorophyll anomaly map for 2017 (Fig. 3.25a). Identical calculations were performed on MODISA sea surface temperature (°C) data to produce an equivalent SST annual mean anomaly (Fig. 3.25b), used to illustrate the relationships between Chl*a* and SST anomalies (Fig. 3.25c). Here the permanently stratified ocean (PSO) is defined as the region where annual average surface temperatures are > 15°C (black lines in Figs. 3.24 and 3.25) and is characterized by surface mixed layers that are typically low in nutrients and shallower than the nutricline (Behrenfeld et al. 2006).

Consistent with the establishment of weak La Niña conditions through much of 2017, Chl*a* concentrations along the equatorial Pacific were neutral to slightly elevated (<10%) above the climatological mean (Fig. 3.25a), reflecting the return of cooler, more nutrient-rich waters conducive to phytoplankton growth. Chl*a* concentrations throughout much of the tropical Pacific, however, were generally diminished relative to climatological values (10%–30%) and inversely related to SST anomalies (gray areas above and below the equator in Fig. 3.25c). Annual mean SST anomalies (Fig. 3.25b) generally coincide with surface mixed layer depth (MLD) anomalies in the PSO, with warmer temperatures associated with shallower mixing, such that phytoplankton spend more time near the ocean's surface and thus have higher daily sunlight exposures than deeper mixing populations. Phytoplankton respond to this increased light by decreasing their cellular chlorophyll levels (Behrenfeld et al. 2016). A secondary consequence of decreased MLD is a decrease in the vertical transport of nutrients to the surface layer, but coupling between the MLD and nutricline depths throughout much of the PSO is known to be weak (Lozier et al. 2011). Modestly depressed Chl*a* concentrations (< 10%) were also observed throughout the Sargasso Sea and in the Mediterranean in 2017. Strongly elevated Chl*a* concentrations were observed in the northern reaches of the North Atlantic (>30%), with weaker increases observed throughout much of the South Atlantic and Indian Ocean regions. Within the boundaries of the PSO, an inverse relationship was generally observed between Chl*a* and SST anomalies (light blue and gray colors in Fig. 3.25c), with some notable exceptions of positive correlations between Chl*a* and SST anomalies in the South Atlantic and southwestern Pacific (dark blue colors in Fig. 3.25c). In regions outside the PSO, no clear relationship was observed between Chl*a* and SST anomalies (Fig. 3.25c), consistent with previous studies (e.g., Behrenfeld et al. 2006; Franz et al. 2017).

Over the 20-year time series of spatially integrated monthly mean Chl*a* values for the PSO (Fig. 3.26a) mean concentrations varied by ~20% (±0.03 mg m^{-3}) around a long-term average of ~0.14 mg m^{-3}. This variability includes significant seasonal cycles in

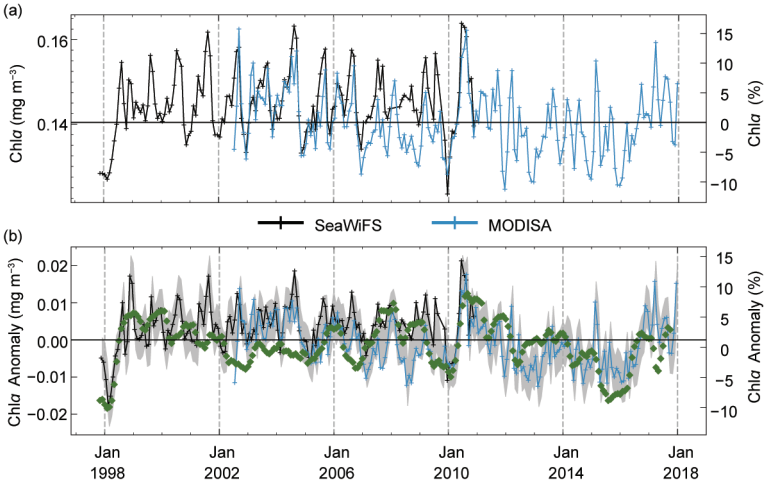

Fig. 3.26. 1998–2017, multimission record of Chl*a* averaged over the PSO for SeaWiFS (black) and MODISA (blue). (a) Independent record from each mission, with horizontal black line indicating the multimission mean Chl*a* concentration for the region (mg m^{-3}). (b) Monthly anomaly (%) for SeaWiFS and MODISA after subtraction of the 9-year MODISA monthly climatological mean (2003–11) from each mission record. The gray region in (b) shows the averaged difference between SeaWiFS and MODISA over the common mission lifetime. Green diamonds show the MEI, inverted and scaled to match the range of the Chl*a* anomalies.

Chl*a* distributions and responses to climatic events. The time series also demonstrates the high level of consistency between the overlapping periods of the SeaWiFS and MODISA missions, lending confidence to interpretation of the multimission record.

Chl*a* monthly anomalies within the PSO (Fig. 3.26b) show variations of ±15% (±0.02 mg m^{-3}) over the multimission time series. For 2017, these anomalies were relatively constant and slightly elevated (+0.005 mg m^{-3}, on average) relative to the long-term mean, consistent with the weak La Niña conditions as discussed previously. The link between ENSO variability and mean Chl*a* response in the PSO is demonstrated by the correspondence of anomaly trends with the multivariate ENSO index (MEI; Wolter and Timlin 1998; Fig. 3.26b, green diamonds, presented in the inverse to illustrate the covariation). From 1997 through 2017, monthly anomalies in Chl*a* concentration within the PSO continue to track large-scale climate oscillations as captured by the MEI (Fig. 3.26b), with some notable deviations in the 2002–06 period.

Variability and trends in Chl*a* reflect both adjustments in phytoplankton biomass and physiology (or health). Both of these properties are mechanistically linked to physical properties of the upper ocean, as well as ecological relationships between phytoplankton and their zooplankton predators. Unraveling the diversity and covariation of factors that influence Chl*a* concentrations is essential for correctly interpreting the implications of Chl*a* anomalies on ocean biogeochemistry and food webs. For example, inverse relationships between Chl*a* and SST can emerge from changes in either mixed-layer light levels or vertical nutrient flux, but these two mechanisms have opposite implications on phytoplankton NPP (Behrenfeld et al. 2016). An additional complication is that measured changes in ocean color often contain a contribution from colored dissolved organic matter (Siegel et al. 2005) that can be mistakenly attributed to changes in Chl*a* (Siegel et al. 2013). Thus, while the satellite record of ocean color continues to provide critical insights on global processes, ongoing effort and new approaches are needed to fully understand the story these data are telling regarding relationships between climate and marine ecosystems.

j. Global ocean carbon cycle—R. A. Feely, R. Wanninkhof, B. R. Carter, P. Landschützer, A. Sutton, and J. A. Triñanes

As a consequence of humankind's collective release of CO_2 emissions into the atmosphere from fossil fuel burning, cement production, and land use changes over the last 250 years, referred to as Anthropogenic CO_2 (C_{anth}), the atmospheric CO_2 has risen from pre-industrial levels of about 278 ppm (parts per million) to about 405 ppm (see Section 2g1). The atmospheric concentration of CO_2 is now higher than has been observed on Earth for at least the last 800 000 years (Lüthi et al. 2008). As discussed in previous *State of the Climate* reports, the global ocean is a major sink for C_{anth}. Here the discussion is updated to include recent estimates of that sink. Over the last decade the global ocean has continued to take up a substantial fraction of the anthropogenic carbon (C_{anth}) emissions and therefore is a major mediator of global climate change. Of the 10.7 (±0.9) Pg C yr^{-1} C_{anth} released during the period 2007–16, about 2.4 (±0.5) Pg C yr^{-1} (26%) accumulated in the ocean, 3.0 (±0.8) Pg C yr^{-1} (30%) accumulated on land, and 4.7 (±0.1) Pg C yr^{-1} (43%) remained in the atmosphere with an imbalance of 0.6 Pg C yr^{-1} (Le Quéré et al. 2018). This decadal ocean carbon uptake estimate is a consensus view based on a combination of measured decadal inventory changes, models, and global air–sea CO_2 flux estimates based on surface ocean partial pressure of CO_2 (pCO_2) measurements. Using ocean general circulation models that include biogeochemical parameterizations (OBGCMs) and inverse models that are validated with observations-based air–sea exchange fluxes and basin-scale ocean inventories, Le Quéré et al. (2018) have demonstrated that the oceanic anthropogenic carbon sink has grown from 1.0 (±0.5) Pg C yr^{-1} in the decade of the 1960s to 2.6 (±0.5) Pg C yr^{-1} in 2016. Air–sea CO_2 flux studies reported here indicate an ocean uptake of C_{anth} of 2.6 Pg C yr^{-1} for 2017.

1) Air–sea carbon dioxide fluxes

Ocean uptake of C_{anth} can be estimated from the net air–sea CO_2 flux derived from the bulk flux formula with air–sea differences in CO_2 partial pressure (ΔpCO_2) and gas transfer coefficients as input. A steady contribution of carbon from riverine runoff, originating from organic and inorganic detritus from land, estimated at 0.45 Pg C yr^{-1} (Jacobson et al. 2007) is included to obtain the C_{anth} uptake by the ocean. The data sources for pCO_2 are annual updates of surface water pCO_2 observations from the Surface Ocean CO_2 Atlas (SOCAT) composed of mooring and ship-based observations (Bakker et al. 2016) and the LDEO database with ship-based observations (Takahashi et al. 2018). The increased observations and improved mapping techniques such as neural network methods and self-organizing maps (Landschützer et al. 2013, 2014; Rödenbeck et al. 2015) provide global pCO_2 fields on a 1° latitude × 1° longitude grid at monthly time scales annually. This allows investigation of

variability on subannual to decadal time scales. The ΔpCO_2 and a parameterization of the gas transfer with wind described in Wanninkhof (2014) are used to calculate the air–sea CO_2 fluxes.

The monthly 2017 ΔpCO_2 maps are based on an observation-based neural network approach of Landschützer et al. (2013, 2014). The 2017 values are projections based on surface temperature, sea surface salinity, climatological mixed-layer depth, satellite chlorophyll-α, atmospheric CO_2, and the neural network for pCO_{2w} developed from the data from the previous decade. Moreover, winds from 2016 are used. A comparison of the 2016 air–sea estimate using wind speeds from 2015, as presented in last year's *State of the Climate* report, and the 2016 global flux using measured 2016 pCO_{2w} and 2016 winds show agreement on a global scale to within 0.1 Pg C yr^{-1}. Changes in winds over time have a small effect on global air–sea CO_2 fluxes (Wanninkhof and Triñanes 2017). The C_{anth} fluxes from 1982 to 2017 suggests a decreasing ocean sink in the first part of the record and a strong increase from 2001 onward that continued into 2017 (Fig. 3.27). The amplitude of seasonal variability is large (≈ 1 Pg C) compared to the long-term trend with minimum uptake in the June–September timeframe. The C_{anth} air–sea flux of 2.6 Pg C yr^{-1} in 2017 is 36% above the 2005–15 average of 1.9 (±0.5) Pg C yr^{-1}.

The average fluxes in 2017 (Fig. 3.28a) show the characteristic pattern of effluxes in the tropical regions and uptake at higher latitudes. The region with largest efflux is the equatorial Pacific. Localized hotspots of upwelling include the Arabian Sea, off the coast of Mauritania, and the Peruvian upwelling system. Large sinks are observed poleward of the subtropical fronts, and the frontal position determines the location of the maximum that is farther south in the Pacific sector of the Southern Ocean compared to the other basins.

In the Northern Hemisphere, there is a significant asymmetry in the sub-Arctic gyre with the North Atlantic being a large sink while the North Pacific is a source of CO_2. Ocean carbon uptake anomalies (Fig. 3.28b) in 2017 relative to a 1995–2015 average are attributed to the increasing ocean CO_2 uptake with time (Fig. 3.27) and to variations in large-scale climate modes. The air–sea flux trend since 2000 is −0.8 Pg C $decade^{-1}$, which leads to predominantly negative flux anomalies (greater ocean uptake). Despite this strong trend there are several regions

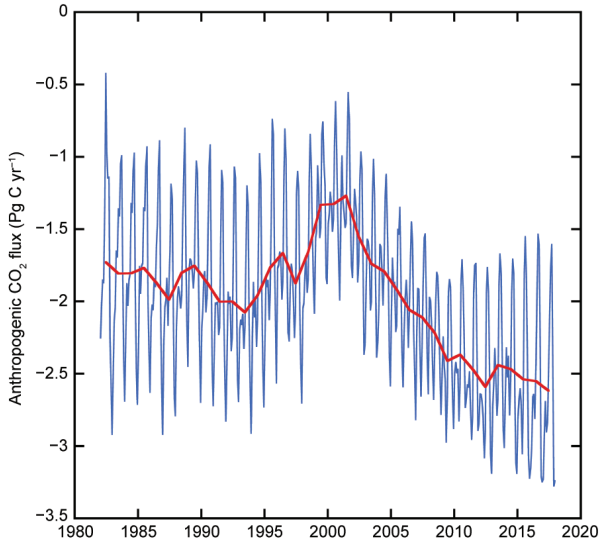

Fig. 3.27. Global annual (red line) and monthly (blue line) C_{anth} fluxes (Pg C yr^{-1}) for 1982 to 2017. Negative values indicate CO_2 uptake by the ocean.

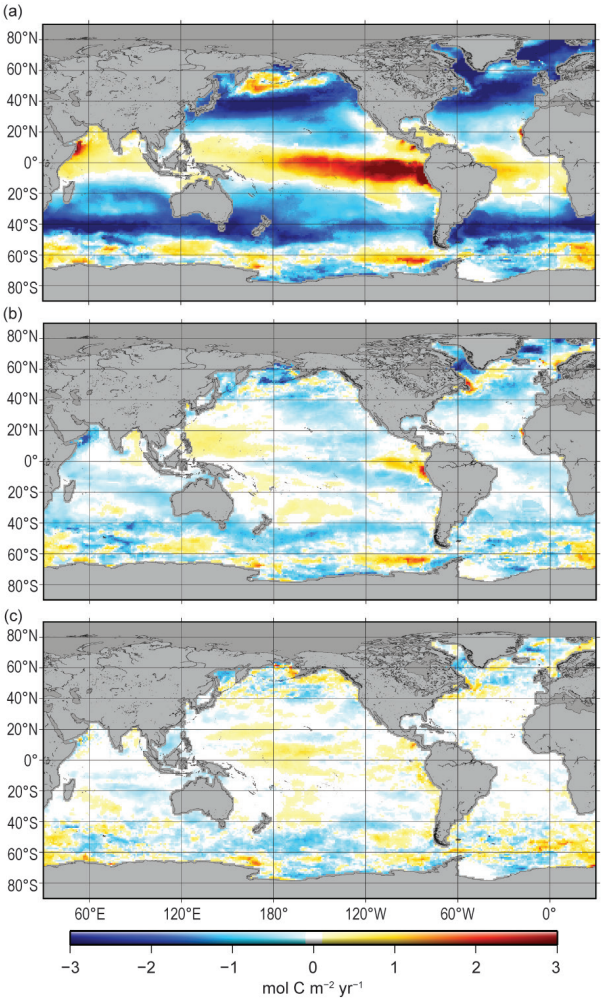

Fig. 3.28. Global map of (a) net air–sea CO_2 fluxes for 2017, (b) net air–sea CO_2 flux anomalies for 2017 relative to a 1995–2015 average, and (c) net air–sea CO_2 flux anomalies for 2017 minus 2016 values following the method of Landschützer et al. (2013), all in mol C m^{-2} yr^{-1}.

showing positive anomalies for 2017, notably the eastern equatorial and western tropical Pacific. The increased effluxes in the eastern equatorial Pacific are related to a predominant positive sign of the ENSO index and the associated switch from the 2015/16 El Niño to the weak La Niñas at the ends of 2016 and 2017. Weaker effluxes in the western tropical Pacific are related to strongly positive PDO values over the past three years that have persisted into the first half of 2017 and associated warmer SSTs.

The differences between the air–sea CO_2 fluxes in 2017 compared to 2016 (Fig. 3.28c) are relatively small. The increase in CO_2 effluxes in the western tropical Pacific from 2016 to 2017 is associated with anomalously warm temperatures in this region in 2017. The Southern Ocean (south of 40°S) shows a bimodal pattern with increasing fluxes in the Pacific and decreasing fluxes in the Atlantic for 2017 compared to 2016. This broadly corresponds to the temperature anomalies in this region, with greater uptake in 2017 associated with warmer temperatures attributed to less upwelling of cold high-CO_2 waters in the western and central Pacific sector of the Southern Ocean and overall colder patterns in the eastern Pacific, Indian, and Atlantic sectors of the Southern Ocean associated with increased ventilation and associated effluxes. The alternating patterns of stronger and weaker uptake in the Southern Ocean are in accord with an asymmetric distribution of the atmospheric pressure systems moving around the Southern Ocean associated with the Antarctic Circumpolar Wave (Landschützer et al. 2015).

Many of the pCO_2 and flux anomalies can be attributed to variations in large-scale climate modes and associated physical anomalies, notably temperature, but the causality is often complex. For example, the behavior of pCO_2 with respect to temperature includes competing processes: thermodynamics dictate decreasing pCO_2 with decreasing SST, but waters originating from the deep with a cold temperature signal will have a high pCO_2. Moreover, the drawdown of pCO_2 due to biology is often associated with increasing temperature, but this depends on region and season.

The strong trend of increasing CO_2 uptake since 2002 has continued through 2017 with an increase of 0.1 Pg C above the 2016 estimate. This increase is well within the uncertainty of the estimate, but it is within the overall expectation that the ocean will remain an increasing sink as long as atmospheric CO_2 levels continue to rise. The sequestration of CO_2 by the ocean partially mitigates the atmospheric CO_2 rise but it comes at a cost of increased acidification of surface and subsurface waters.

2) Ocean acidification

To date, the global oceans have absorbed approximately 150 (±20) Gt C of the total anthropogenic carbon dioxide emissions (Le Quéré et al. 2018). This uptake has caused an increase of ocean acidity in a process referred to as anthropogenic ocean acidification (OA). Models indicate that over the last two-and-a-half centuries, the pH in open-ocean surface waters has decreased by about 0.11 units, equivalent to about a 29% increase in the hydrogen ion (H+) concentration (Gattuso et al. 2015). This absorption of anthropogenic carbon is beneficial in slowing the rise of atmospheric carbon dioxide. However, the ocean's uptake of carbon dioxide is having negative impacts on ocean chemistry and biology. Time series measurements, hydrographic surveys, and modeling studies have revealed that the changes in seawater chemistry resulting from the absorption of CO_2 are lowering seawater pH. For example, the time series data at Ocean Station ALOHA shows an average pH decrease of approximately 0.02 units decade^{-1} in the northeast Pacific (Fig. 3.29).

The long-term trend at Ocean Station ALOHA shows an increasing rate of increase of pCO_2 of 2.0 (±0.1) μatm yr^{-1} (Fig. 3.29a) while pH of ocean surface waters has already decreased by about 0.0016 yr^{-1}, with no apparent long-term change in annual CO_2 influx (Fig. 3.29b; Sutton et al. 2017). The increase in surface ocean CO_2 over recent decades is consistent with the atmospheric increase within the statistical limits of the measurements.

3) Carbon inventories

The Global Ocean Ship-based Hydrographic Investigations Program (GO-SHIP) is providing new information about the uptake and storage of carbon within the ocean interior by determining the change in measured dissolved inorganic carbon (DIC) and C_{anth} concentrations between decadal cruise reoccupations. During the 2017/18 timeframe, a new set of measurements, including DIC, were finalized along the P18 line extending from San Diego south to Antarctica and collected along the P06 line extending from Australia east to Chile. A synthesis of estimates of C_{anth} storage along these sections and other recently measured Pacific sections is currently underway. While results are preliminary, the dominant signal is a clear and continuous increase in C_{anth} storage, especially in the least-dense and most well-ventilated shallower parts of the ocean (Fig. 3.30a). This C_{anth} storage is increasing ocean acidity, decreasing ocean

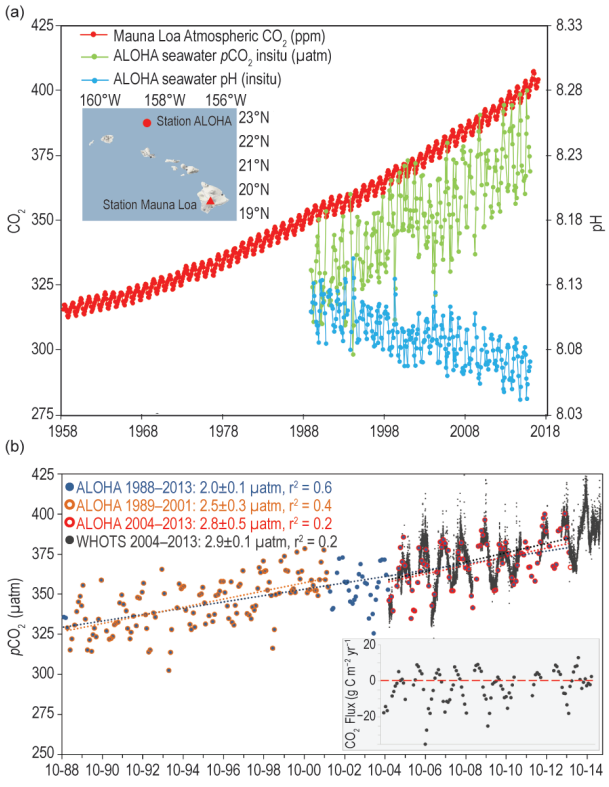

Fig. 3.29. (a) Time series of atmospheric CO_2 at Mauna Loa (ppm), surface ocean pCO_2 (µatm) and pH at Ocean Station ALOHA in the subtropical North Pacific Ocean. Mauna Loa data: (ftp://aftp.cmdl.noaa.gov/products/trends/co2/co2_mm_mlo.txt); HOTS/ALOHA data: University of Hawaii (http://hahana.soest.hawaii.edu/hot/products/HOT_surface_CO2.txt). (b) Surface ocean pCO_2 (µatm) and rates of change from Station ALOHA 1988–2013 (blue), 1989–2001 (orange), 2004–13 (red), and the adjacent WHOTS buoy 2004–13 (black) and (shaded inset) CO_2 flux (g C m^{-2} yr^{-1}) from WHOTS buoy observations 2004–15 (after Sutton et al. 2017).

pH (Fig. 3.30b), and decreasing carbonate mineral saturation states. For this comparison, anthropogenic CO_2 storage rates—estimated from decadal measurements using methods described by Carter et al. (2017)—are used directly and, in some regions, extrapolated in time to estimate patterns of C_{anth} storage since 1994. These storages are added to the 1994 global C_{anth} climatology of Sabine et al. (2004) as gridded by Key et al. (2004).

As also found in recent studies in the Atlantic (Woosley et al. 2016) and Pacific (Carter et al. 2017), these preliminary results suggest that Pacific storage rates have been increasing since ~2005 despite the tendency of water with more CO_2 to absorb smaller fractions of atmospheric C_{anth} increases (due to the decreasing buffering capacity of seawater). The observed storage increases are attributable to continued rapid atmospheric CO_2 growth and changes in mixing and ventilation within the ocean interior. The largest storages per unit area are found in high-latitude deep water formation regions such as the North Atlantic (Woosley et al. 2016), though the majority of the C_{anth} inventory is stored in the subtropics due to the vast size of that region. Upwelling regions near the equator, in the North Pacific, and in the Southern Ocean south of the Antarctic Circumpolar Current have lower decadal storages per unit area (e.g., the dark colors on the lower right Section in Fig. 3.30a). In these regions, upwelling of deep waters that have been isolated from the atmosphere for all or some of the industrial era displace the better-ventilated, higher C_{anth} intermediate depth waters. A preliminary estimate of the decadal changes suggests that the Pacific basin stored 8.2 Pg C between 1995 and 2005 and 9.8 Pg C between 2005 and 2015.

Ocean acidification, or the impact of C_{anth} on pH, has a similar global pattern to the net C_{anth} storage, though the pH decrease is amplified in seawater with

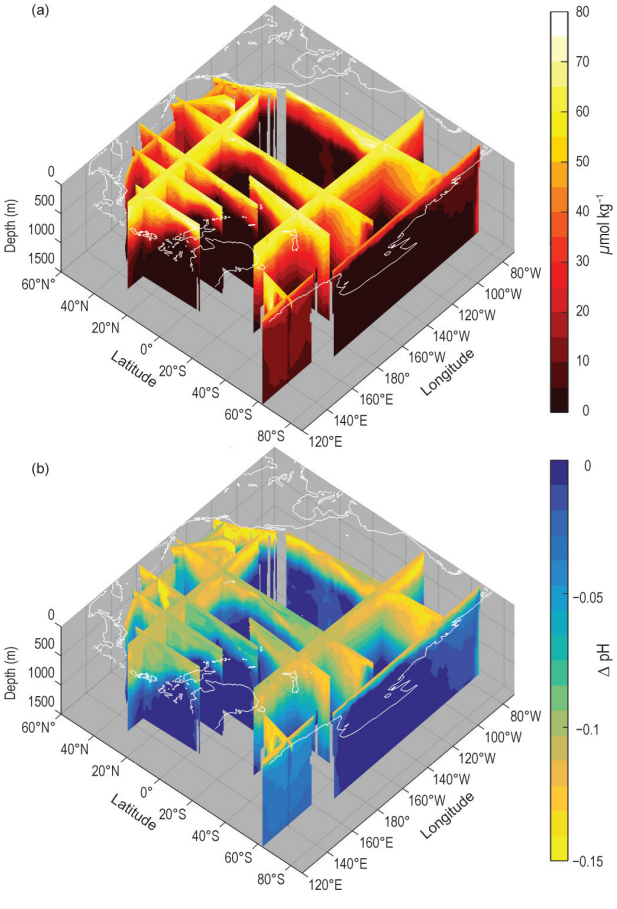

Fig. 3.30. Preliminary estimates of (a) anthropogenic carbon (C_{anth}; µmol kg^{-1}) along hydrographic sections in the Pacific interpolated (or extrapolated) in time to the year 2015 and (b) the net impact of this C_{anth} on pH.

naturally high accumulated DIC from respiration by marine organisms. Such waters have a reduced buffer capacity due to their naturally high carbon concentrations, so the ongoing C_{anth} storage has an enhanced impact on acidification. This effect can be seen in the nearly global subsurface ΔpH magnitude maximum, which is especially notable off the US West Coast where unusually high-DIC waters upwell near the surface (Fig. 3.30b).